

The rp Process Ashes from Stable Nuclear Burning on an Accreting Neutron Star

Hendrik Schatz¹, Lars Bildsten and Andrew Cumming

Department of Physics and Department of Astronomy
366 LeConte Hall, University of California, Berkeley, CA 94720
email: h.schatz@gsi.de, bildsten@fire.berkeley.edu, cumming@fire.berkeley.edu

Michael Wiescher

Department of Physics, University of Notre Dame, Notre Dame, IN 46556
email: wiescher.1@nd.edu

ABSTRACT

The temperature and nuclear composition of the crust and ocean of an accreting neutron star depend on the mix of material (the ashes) that is produced at lower densities by fusion of the accreting hydrogen and helium. The hydrogen/helium burning is thermally stable at high accretion rates, a situation encountered in weakly magnetic ($B \ll 10^{11}$ G) neutron stars accreting at rates $\dot{M} > 10^{-8} M_{\odot} \text{ yr}^{-1}$ and in most accreting X-ray pulsars, where the focusing of matter onto the magnetic poles results in local accretion rates high enough for stable burning. For a neutron star accreting at these high rates, we calculate the steady state burning of hydrogen and helium in the upper atmosphere ($\rho < 2 \times 10^6 \text{ g cm}^{-3}$), where $T \approx (5\text{--}15) \times 10^8 \text{ K}$. Since the breakout from the “hot” CNO cycle occurs at a temperature comparable to that of stable helium burning ($T \gtrsim 5 \times 10^8 \text{ K}$), the hydrogen is always burned via the rapid proton capture (rp) process of Wallace and Woosley.

The rp process makes nuclei far beyond the iron group, always leading to a mixture of elements with masses $A \sim 60\text{--}100$. The average nuclear mass of the ashes is set by the extent of helium burning via (α, p) reactions, and, because these reactions are temperature sensitive, depends on the local accretion rate. Nuclear statistical equilibrium, leading to a composition of mostly iron, occurs only for very high local accretion rates in excess of 50 times the Eddington rate.

We briefly discuss the consequences of our results for the properties of the neutron star. The wide range of nuclei made at a fixed accretion rate and the sensitivity of the ash composition to the local accretion rate makes it inevitable that accreting neutron stars have an ocean and crust made up of a large variety of nuclei. This has repercussions for the thermal, electrical and structural properties of the neutron star crust. A crustal lattice as impure as implied by our results will have the conductivity throughout most of its mass set by impurity scattering, allowing for more rapid Ohmic diffusion of magnetic fields than previously estimated for mono-nuclear mixes.

Subject headings: accretion – dense matter – nuclear reactions, nucleosynthesis, abundances – stars: neutron – X-rays: bursts

To Appear in The Astrophysical Journal

¹ Current address: Gesellschaft für Schwerionenforschung, Darmstadt, Germany

1. Introduction

Neutron stars in mass-transferring binaries accrete hydrogen and helium rich material from their companions at rates ranging from 10^{-11} – $10^{-8} M_{\odot} \text{ yr}^{-1}$. This matter undergoes thermonuclear fusion within hours to days of reaching the neutron star surface, releasing ≈ 5 MeV per nucleon for solar abundances. The nuclear burning is thermally unstable on weakly magnetic neutron stars ($B \ll 10^{11}$ G) accreting at $\dot{M} < 10^{-8} M_{\odot} \text{ yr}^{-1}$ and produces energetic ($\sim 10^{39}$ erg) Type I X-ray bursts when $\dot{M} < 10^{-9} M_{\odot} \text{ yr}^{-1}$ (see Lewin, van Paradijs & Taam 1995 and Bildsten 1998b for recent reviews; observationally, the nature of the time dependent burning in the regime $10^{-9} M_{\odot} \text{ yr}^{-1} < \dot{M} < 10^{-8} M_{\odot} \text{ yr}^{-1}$ is still not understood). The composition of the ashes from the unstable burning is still uncertain, but most certainly consists of heavy nuclei, potentially beyond the iron group (Hanawa, Sugimoto & Hashimoto 1983; Wallace & Woosley 1984; Schatz et al. 1997; Schatz et al. 1998, Koike et al. 1999).

In this paper, we calculate for the first time the mix of nuclei made during *thermally stable* hydrogen/helium burning in the upper atmosphere of an accreting neutron star. This is appropriate for most accreting X-ray pulsars, where the local accretion rate is high enough for stable burning on the magnetic polar cap (Joss & Li 1980; Bildsten & Brown 1997), and for the bright “Z” sources of Hasinger and van der Klis (1989) that are not regular Type I bursters and accrete globally at $\dot{M} \sim 10^{-8} M_{\odot} \text{ yr}^{-1}$. Whereas accurately calculating the ashes from unstable burning requires time-dependent, three-dimensional modelling of the ignition and propagation of the flame, stable burning is time-independent and therefore calculation of the ashes is much more straightforward.

The ashes are forced by accretion into the neutron star ocean and crust, replacing what was there at birth. The ensuing electron captures, neutron emissions and pycnonuclear reactions release energy locally and drive the matter neutron-rich (Bisnovatyi-Kogan & Chechetkin 1979; Sato 1979; Haensel & Zdunik 1990; Blaes et. al. 1990; Bildsten 1998a; Brown, Bildsten & Rutledge 1998). Thus the composition of an accreted or accreting neutron star ocean and crust is very different from the primordial one (see Pethick and Ravenhall 1995 for a recent discussion of the primordial crust) and depends critically on the range and type of nuclei made during the H/He burning in the upper atmosphere. Previous studies of accreting neutron star crusts presumed that iron is the sole product of nuclear burning in the upper atmosphere and is the only nucleus entering the neutron star crust. We find that the hydrogen burning on these rapidly accreting neutron stars is mostly via the rp process of Wallace and Woosley (1981), resulting in a complicated mix of elements, *nearly all much heavier than iron*.

The thin outer crust of a neutron star (before neutron drip at $\rho \approx (4\text{--}6) \times 10^{11} \text{ g cm}^{-3}$) is replaced by accretion of only $\approx 10^{-4} M_{\odot}$ of material. Thus all of the neutron stars in low-mass X-ray binaries should have an accreted outer crust. Indeed these objects accrete enough material to unambiguously replace their *whole* crust (down to the crust/core interface), which is typically a few percent of the total stellar mass (Ravenhall & Pethick 1994). The X-ray pulsars typically accrete from the wind of a massive companion at a rate $\dot{M} \sim 10^{-11}$ – $10^{-10} M_{\odot} \text{ yr}^{-1}$ (see Bildsten et al. 1997 for a recent overview) and so are capable of replacing their outer crusts. A few of these objects (SMC X-1, LMC X-4, Her X-1) are accreting at high enough rates or for long enough times (as inferred by the $2.2 M_{\odot}$ mass companion to Her X-1) to replace their whole crust.

Knowledge of the composition and thermal properties of an accreting neutron star’s ocean and crust is important for many studies. For example, the temperature and composition of the crust affects the thermal conductivity and the Ohmic diffusion time there (see Brown & Bildsten 1998 for a recent application/overview of this problem). The crustal composition determines the amount of heat deposited directly

in the crust (Haensel & Zdunik 1990; Miralda-Escude et al. 1990) and the rate of neutrino emission from the crust (Haensel, Kaminker & Yakovlev 1996), both of which are important for finding the equilibrium core temperature of an accreting neutron star (Fujimoto et al. 1984; Brown & Bildsten 1998). The predicted frequencies of the so-far unobserved ocean g-modes depend directly on the average nuclear mass (Bildsten & Cutler 1995; Bildsten & Cumming 1998).

We begin in §2 with an introduction to the basic equations we solve and a summary of the input microphysics. In §3, we discuss the high accretion rate burning regime and explain why the burning is thermally stable at high accretion rates and why the helium ignites in a hydrogen-rich environment, thus providing an excellent site for the rp process. In §4, we explain the overall thermal and compositional structure of the burning layer and provide convenient analytic expressions for the temperature and depth of the burning. Section 5 contains an in-depth discussion of the nature of the rp process. We explain how the burning depends on the local accretion rate, with particular emphasis on the important role of the α p process in determining the final average mass of the nuclei. We conclude in §6 with a summary of our work and some speculations about how these results will impact studies of the neutron star crust and ocean. In the Appendix, we describe how we calculate the radiative and conductive opacities for the complex mixtures produced by the hydrogen/helium burning.

2. Basic Equations and Microphysics

The plane-parallel nature of the neutron star atmosphere means that the physics of nuclear burning depends on the accretion rate per unit area, \dot{m} (Fujimoto, Hanawa & Miyaji 1981, hereafter FHM). This parameter determines the local behavior on the neutron star and need not be the same everywhere, especially on accreting X-ray pulsars. The local zero metallicity Eddington rate (the accretion rate at which the outgoing radiation exerts a force comparable to gravity) is

$$\dot{m}_{\text{Edd}} = \frac{2m_p c}{(1+X)R\sigma_{\text{Th}}} = 8.8 \times 10^4 \text{ g cm}^{-2} \text{ s}^{-1} \left(\frac{1.71}{1+X} \right) \left(\frac{10 \text{ km}}{R} \right), \quad (1)$$

where σ_{Th} is the Thomson scattering cross-section, m_p is the proton mass, c is the speed of light, X is the hydrogen mass fraction, and R is the stellar radius. In this paper, we use the Eddington accretion rate for solar composition ($X = 0.71$) and $R = 10 \text{ km}$, $\dot{m}_{\text{Edd}} = 8.8 \times 10^4 \text{ g cm}^{-2} \text{ s}^{-1}$, as our basic unit for the local accretion rate.

Steady accretion modifies the equations of particle continuity and entropy for a hydrostatic settling atmosphere (FHM; Brown & Bildsten 1998). We write these equations in a coordinate system of fixed pressure P , so that the accreted matter flows through the coordinates as it is compressed by accretion of fresh material from above. Hydrostatic balance (the ram pressure of the accretion flow is negligible) yields $P = gy$, where the column depth y (in g cm^{-2}) is defined by $dy = -\rho dz$, and $g \approx GM/R^2$ (we neglect general relativistic corrections). The continuity equation for an element i (with number density n_i) is

$$\frac{\partial n_i}{\partial t} + \nabla \cdot (n_i \mathbf{v}) = \sum r, \quad (2)$$

where $\sum r$ is the summed rates of particle creation and destruction processes. For these high accretion rates, there is not time for differential settling and all elements co-move downward at the speed needed to satisfy mass continuity, $v = \dot{m}/\rho$ (Wallace, Woosley & Weaver 1982; Bildsten, Salpeter & Wasserman 1993). We define a mass fraction $X_i \equiv \rho_i/\rho = A_i m_p n_i/\rho$ where A_i is the baryon number of species i and expand the

continuity equation to obtain

$$\frac{\partial X_i}{\partial t} + \dot{m} \frac{\partial X_i}{\partial y} = \frac{A_i m_p \sum r}{\rho}. \quad (3)$$

The equation for the entropy is

$$T \frac{ds}{dt} = -\frac{1}{\rho} \nabla \cdot \mathbf{F} + \epsilon, \quad (4)$$

where ϵ is the energy release rate from nuclear burning and \mathbf{F} is the heat flux. We write the entropy as $Tds = C_p T(dT/T - \nabla_{\text{ad}} dP/P)$, where $\nabla_{\text{ad}} = d \ln T / d \ln P$ for an adiabatic change and C_p is the specific heat at constant pressure. Since the temperature can depend on both time and pressure, we find

$$\frac{\partial F}{\partial y} + \epsilon = C_p \left(\frac{\partial T}{\partial t} + \dot{m} \frac{\partial T}{\partial y} \right) - \frac{C_p T \dot{m}}{y} \nabla_{\text{ad}}. \quad (5)$$

Equations (3) and (5) describe the hydrostatic evolution of the neutron star atmosphere while constantly accreting. In our steady-state calculations, we neglect the time-dependent terms in these equations.

We solve the continuity and entropy equations in connection with a nuclear reaction network to determine the nuclear energy generation rate ϵ in equation (5) and the nuclear abundances $Y_i \equiv X_i/A_i$. The nuclear reaction network used here is described in detail in Schatz et al. (1998) and the references therein (see also Herndl et al. 1995, Van Wormer et al. 1994, and Wiescher et al. 1986 for discussions of the reaction rates). The network includes 631 nuclei between hydrogen and ^{100}Sn covering the range from stability to the proton drip line. The types of reactions considered are all proton, neutron and α induced reactions as well as photodisintegration, β^+ decay and electron capture. For most nuclei in the range $Z \leq 32$ and $A \leq 60$ the temperature and density dependent weak interaction rates are taken from the compilation of Fuller, Fowler & Newman (1980, 1982a, 1982b). These weak interaction rate data include energy losses due to emission of neutrinos in electron captures and β^+ decays. Since similar data for heavier nuclei are not available, the β -decay rates of nuclei with $Z > 32$ were approximated using temperature and density independent earth rates (for a justification see Schatz et al. 1998). Energy loss via neutrinos is neglected for these nuclei. Electron captures do not play an important role for the density regime in which we work. Electron screening is treated according to Graboske et al. (1973) and Itoh et al. (1979).

For the equation of state, we assume the ions behave as an ideal gas (Coulomb corrections to the ion equation of state are unimportant at the column depths of interest to us) and we use the interpolation formulae of Paczynski (1983) to account for the partially degenerate electrons. The heat flux through the atmosphere is given by

$$F = -\frac{c}{3\kappa\rho} \frac{d}{dz} aT^4 = \frac{c}{3\kappa} \frac{d}{dy} aT^4, \quad (6)$$

where a is the radiation constant. The opacity κ is set by electron scattering, free-free absorption and conduction. In the Appendix, we discuss in detail how we calculate each of these contributions for the complex mixtures produced by the hydrogen/helium burning.

We assume an initial solar composition (Anders and Grevesse 1989) of the accreted material and a neutron star with $M = 1.4 M_\odot$ and $R = 10$ km. The influence of these parameters on our results is discussed later. The only boundary condition that has to be chosen is the radiation flux exiting the top of the atmosphere. For these steady-state models at high accretion rates, the flux is dominated by the nuclear energy release from the conversion of hydrogen and helium to heavy elements (≈ 5 MeV per nucleon). There is also energy release from gravitational settling and energy generated in the crust due to electron captures, neutron emission and pycnonuclear reactions (see Brown & Bildsten 1998 for a discussion of this issue). However, these contributions to the flux are small ($\lesssim 10\%$) compared to the nuclear energy release, and we

do not include them here. In particular, we drop the terms proportional to C_p on the right-hand side of equation (5). Our approach is to guess the flux at the top of the atmosphere, integrate to the base of the burning layer and then compare the flux generated by the nuclear burning to our initial estimate. We find that this procedure converges to give the correct upper boundary condition in only a few iterations.

3. The Nature of Hydrogen and Helium Burning at High Accretion Rates

For the high accretion rates of interest to us, the temperature at the depth where burning occurs is always in excess of 8×10^7 K, so the hydrogen burns either via the hot CNO cycle or, at the higher temperatures at later stages, via the rp process. During the hot CNO cycle the timescale for proton captures is shorter than that for subsequent β decays. The time to go around the catalytic loop is set by the β decay lifetimes of ^{14}O ($t_{1/2} = 70.6$ s) and ^{15}O ($t_{1/2} = 122.2$ s) and is *temperature independent*. The β -decays fix the hydrogen burning rate at (Hoyle & Fowler 1965)

$$\epsilon_{\text{CNO}} = 5.8 \times 10^{15} Z_{\text{CNO}} \text{ ergs g}^{-1} \text{ s}^{-1}, \quad (7)$$

where Z_{CNO} is the mass fraction of CNO in the accumulating matter. The timescale to consume all of the hydrogen is then $\approx 790 \text{ s}/Z_{\text{CNO}}$ or about one day for solar metallicity. For high accretion rates (especially when the burning is stable), the matter reaches high enough temperatures for helium ignition before the hydrogen has been exhausted. The helium burning then occurs in a hydrogen rich environment (Lamb & Lamb 1978; Taam & Picklum 1978, 1979; FHM; Taam 1982).

For normal or sub-solar metallicities and accretion rates in the regime $10^{-10} M_{\odot} \text{ yr}^{-1} \lesssim \dot{M} \lesssim 10^{-8} M_{\odot} \text{ yr}^{-1}$, the helium ignition is thermally unstable and results in a Type I X-ray burst. At higher accretion rates, the helium burns at a temperature ($T \gtrsim 5 \times 10^8$ K) where the burning is *thermally stable* because the nuclear energy generation rate is less temperature sensitive than the radiative cooling (FHM). This allows a rough estimate of the critical accretion rate \dot{m}_{st} where the burning becomes stable (Bildsten 1998b),

$$\dot{m}_{st} \approx 1.3 \times 10^5 \text{ g cm}^{-2} \text{ s}^{-1} \left(\frac{M}{1.4 M_{\odot}} \right)^{1/2} \left(\frac{10 \text{ km}}{R} \right), \quad (8)$$

in which we take a nominal value $\kappa = 0.4\kappa_{es}$, where $\kappa_{es} = \sigma_{\text{Th}}(1 + X)/2m_p$ is the Thomson scattering opacity. Bildsten (1998b) recently reviewed the accretion rate regimes originally introduced by FHM. The high local accretion rates of the X-ray pulsars are the standard argument as to why they don't burst (Joss & Li 1980, Bildsten & Brown 1997).

The simple calculation which gives equation (8) is not accurate enough to say whether \dot{m}_{st} is above or below the Eddington rate. FHM estimated \dot{M}_{st} (they called it \dot{M}_{cri} in their Table 1) for 3 different neutron stars (here $\dot{M} = 4\pi R^2 \dot{m}$). They found $\dot{M}_{st}/(10^{-9} M_{\odot} \text{ yr}^{-1}) = 15, 13, \text{ and } 12$ for $M = 0.476, 1$ and $1.41 M_{\odot}$. Equation (8) agrees to within 20–30%, giving $\dot{M}_{st}/(10^{-9} M_{\odot} \text{ yr}^{-1}) = 13, 16, \text{ and } 17$ for the same three masses and radii. To accurately determine if the burning is thermally stable requires solving the time-dependent equations numerically. Ayasli & Joss (1982) and Taam, Woosley & Lamb (1996) performed time-dependent calculations at accretion rates comparable to the Eddington limit and found that the burning is thermally unstable when $\dot{M} < \dot{M}_{\text{Edd}}$. Ayasli & Joss (1982) also carried out some calculations with super-Eddington accretion rates (by a factor of a few) and found thermal stability. However, there has not been a thorough survey of the dependence of the critical accretion rate \dot{m}_{st} on M , R and composition.

Our focus in this paper is calculating the nucleosynthesis when the burning is thermally stable. In this regime, the helium is consumed over a time interval of less than 20 minutes and the resulting enhancement

of the number of CNO seed nuclei together with breakout from the CNO cycle leads to a rapid consumption of hydrogen via the rp process.

4. Steady-State Burning Models: Helium Ignition as the Hydrogen Burning Trigger

Steady-state burning of hydrogen and helium takes place in three phases: hydrogen burning via the hot CNO cycle at low densities (§3), mixed hydrogen and helium burning via the 3α reaction and the α p and rp processes when helium ignites (§§4 and 5), and pure helium burning via α captures after the exhaustion of hydrogen (§5.5). For all accretion rates where the burning is in steady-state, consumption of hydrogen by the hot CNO cycle is unimportant before the helium ignites. It is helium ignition which acts as the trigger for hydrogen burning. To understand this, we write the depth at which hydrogen would be consumed by the hot CNO cycle as $y_{\text{CNO}} = \dot{m}E_{\text{CNO}}/\epsilon_{\text{CNO}}$, or, using equation (7),

$$y_{\text{CNO}} = 5.74 \times 10^9 \text{ g cm}^{-2} \dot{m}_5 \left(\frac{Z_{\text{CNO},\odot}}{Z_{\text{CNO}}} \right). \quad (9)$$

For the high accretion rates of interest here, y_{CNO} is always much greater than the column depth at which helium ignites, y_{burn} (see the estimate of y_{burn} in eq. [12] below). Thus the helium ignites before significant amounts of hydrogen are burned by the hot CNO cycle². Rapid consumption of hydrogen by the rp process then follows.

We have calculated steady-state models for local accretion rates between $\dot{m}/\dot{m}_{\text{Edd}} = 0.7$ and 60. The temperature, density and composition as a function of column depth are shown in Figure 1 for four accretion rates, $\dot{m}/\dot{m}_{\text{Edd}} = 1, 5, 20$, and 50, which we will discuss in detail. The steep rise in the mean molecular weight indicates the location of most of the hydrogen burning. Figure 2 shows the opacity κ for these models. The opacity “bump”, particularly prominent at low accretion rates, is due to free-free absorption. This dominates electron scattering after the heavy elements are made and until the opacity is set by electron conduction (see Appendix for a full discussion). Figure 3 shows the temperature-density profiles. The region to the left of the dashed line is where the temperature is high enough so that the positron fraction exceeds 10%. We have safely stayed in the regime where we can neglect positrons, confining our calculations to $\dot{m}/\dot{m}_{\text{Edd}} < 60$. We show later that this limit coincides with the onset of nuclear statistical equilibrium, where the outcome of the nucleosynthesis is simply determined by thermodynamics and does not need to be calculated in detail.

Figure 4 shows the abundances of hydrogen and helium as a function of time and column depth. It is clear that nearly all the hydrogen burning occurs where the helium ignites. We make a simple estimate of this location by matching the helium lifetime to the 3α reaction to the time it takes to cross a scale height. Using the energy generation rate for helium burning via the 3α reaction ($\epsilon_{3\alpha}$), we write $\dot{m}Y/y \approx \epsilon_{3\alpha}/E_{3\alpha}$ (Taam 1981, Fushiki & Lamb 1987, Bildsten 1995) where $E_{3\alpha} = 5.84 \times 10^{17} \text{ ergs g}^{-1}$ is the energy release from $3\alpha \rightarrow {}^{12}\text{C}$. Using the temperature-density relation for an atmosphere with pure Thomson scattering and a constant flux $F = 10^{23} \text{ erg cm}^{-2} \text{ s}^{-1} E_{18} \dot{m}_5$, we find that the helium ignition temperature is given by the solution to

$$\dot{m}_5^4 = 68.2 \left[\frac{(Yg_{14}\mu)^2 T_8^7}{(1+X)^3 E_{18}^3} \right] \exp \left(\frac{-44}{T_8} \right) \quad (10)$$

²This does not change even if we consider breakouts from the hot CNO cycle. We show later in §5.1 that when breakout occurs at high accretion rates, the limited number of available seed nuclei and the short time remaining before the onset of the 3α reaction limits the hydrogen consumption via breakout reactions prior to helium ignition to only 10% of the available fuel.

(Bildsten 1998b), where we write the energy released per gram of accreted material in units of 10^{18} erg g^{-1} as E_{18} and the accretion rate in units of $10^5 \text{g cm}^{-2} \text{s}^{-1}$ as \dot{m}_5 . Solving this transcendental equation for the temperature gives the pressure at which the helium burns and, most importantly, how these quantities depend on \dot{m} , M , R and the abundances. In order to simplify the transcendental, we expand the exponential about the temperature of $T_8 = 6.285$ (in the middle of the range we are interested in) so that $\exp(-44/T_8) \approx 9.11 \times 10^{-4} (T_8/6.285)^7$. Some accuracy is compromised because of this approximation, but not much. We thus find

$$T_{\text{burn}}^{\text{est}} = 3.06 \times 10^8 \text{K} \dot{m}_5^{2/7} \frac{(E_{18} + X E_{18})^{3/14}}{(Y g_{14} \mu)^{1/7}}, \quad (11)$$

and

$$y_{\text{burn}}^{\text{est}} = \frac{3.36 \times 10^7 \text{g cm}^{-2} \dot{m}_5^{1/7}}{(E_{18} + X E_{18})^{1/7} (Y g_{14} \mu)^{4/7}}. \quad (12)$$

as the temperature and column density at the helium burning location.

These estimates compare well with our numerical results (we take $E_{18} = 5.3$, $g_{14} = 1.86$, $\mu = 0.61$, $X = 0.71$, and $Y = 0.28$). Equation (12) accurately gives the location where 10 – 20% of the helium is burned. The temperature estimate is consistently 20% too high (for the same location). We have also checked the dependence of the burning conditions on gravity for a fixed $\dot{m} = 7.5 \times 10^4 \text{g cm}^{-2} \text{s}^{-1}$ model. We find that the burning takes place at higher temperatures, lower densities and higher column depths for a lower gravity, confirming the gravity dependence of equations (11) and (12). Thus our simple estimate accurately reproduces the scalings seen in the numerical simulations.

5. Nucleosynthesis from Mixed Hydrogen and Helium Burning

When the helium ignites, mixed hydrogen and helium burning occurs via the 3α reaction, the αp process and the rp process. The ignition of 3α -burning and subsequent carbon production in a hydrogen rich environment provides additional seeds which accelerate the burning of hydrogen. The αp process is a series of (α, p) reactions and proton captures starting with the $^{14}\text{O}(\alpha, \text{p})^{17}\text{F}$ reaction. This is a pure helium burning process since for each proton released in an (α, p) reaction a proton is captured in a subsequent (p, γ) reaction (Wallace and Woosley 1981). Hydrogen must be present for the αp process to play a role, since proton capture reactions provide the link between the ^{12}C produced by the 3α reaction, and the ^{14}O at the beginning of the αp process. Most of the hydrogen is burned by the rp process (rapid proton capture process), a series of fast proton captures and slow β -decays close to the proton drip line (Wallace and Woosley 1981). We show later that the typical mass of nuclei at the endpoint of the rp process (A_{rp}) is around 60–100 and is determined both by the exhaustion of hydrogen and the prevalence of the αp process.

Before describing our detailed results, we start with a simple picture of the mixed hydrogen and helium burning. Imagine that helium burns only via the 3α reaction and breakout from the hot CNO cycle, for example via the $^{15}\text{O}(\alpha, \gamma)^{19}\text{Ne}$ reaction. Then, ^{19}Ne is the seed nucleus for hydrogen burning via the rp process. Neglecting the small amount of hydrogen burned before helium ignition, for solar abundance there are 38 protons per ^{19}Ne seed nucleus. If there are no catalytic loops, the ensuing rp process would produce nuclei with a typical mass $A_{\text{rp}} \approx 57$ after all the hydrogen is burned. We generalize this simple estimate to the case where helium is burning via the αp process, by assuming that only one endpoint nucleus is produced from the αp process (mass number $A_{\alpha\text{p}}$), which again serves as the seed nucleus for the rp process. The typical mass A_{rp} of the endpoint of the rp process then depends on the mass fraction of helium burned into

seed nuclei for the rp process (Y_{burn}) and the endpoint of the helium burning ($A_{\alpha p}$),

$$A_{\text{rp}} \approx A_{\alpha p} \left(1 + \frac{X}{Y_{\text{burn}}} \right) \quad (13)$$

(Schatz et al. 1998). Thus the strong temperature sensitivity of the (α, p) reactions in the αp process is imprinted on the rp process ashes. In this section, we first describe the physics that determines $A_{\alpha p}$ and show that the temperature at the depth of helium ignition is the most important parameter. We then discuss the rp process and the resulting distribution of elements, and show that equation (13) is a good estimate of our numerical results.

5.1. CNO Breakout and the αp Process

Crucial for the rp process is the extent to which α -induced reactions other than the 3α reaction can take place. The major limiting factor is the Coulomb barrier for the α particles, which increases rapidly towards heavier nuclei. In Figure 5, the dotted line shows the temperatures and densities where the $^{15}\text{O}(\alpha, \gamma)^{19}\text{Ne}$ rate equals the ^{15}O β^+ decay rate. To the right of this line, breakout from the hot CNO cycle can occur. The dashed lines show where the (α, p) reaction rate on ^{14}O , ^{18}Ne , ^{22}Mg , ^{26}Si , ^{30}S and ^{34}Ar equals the rate of destruction (by β^+ decay and proton capture) of each of these isotopes. The αp process will proceed via a particular (α, p) reaction if the temperature and density of a fluid element reach the corresponding threshold (dashed line) during helium burning. Otherwise, the αp process will end and the reaction flow towards heavier nuclei will continue via the rp process.

For nuclei above ^{18}Ne proton captures can in principle compete with α -induced reactions as the proton capture rates are typically much faster than the (α, p) reaction rates. However, at the temperatures where the helium burning occurs, the (γ, p) photodisintegration reactions are in balance with the (p, γ) reactions, which strongly hampers effective proton captures. This does not mean, as it is often concluded, that proton captures are always negligible. In fact, the deviations of the thresholds shown in Figure 5 from the smooth behavior at low densities are due to proton captures. For example, let's consider ^{22}Mg . In this case, the nuclei ^{22}Mg and ^{23}Al are in (p, γ) - (γ, p) equilibrium determined by the Saha equation. However, the $^{23}\text{Al}(p, \gamma)^{24}\text{Si}$ reaction operating on the low ^{23}Al equilibrium abundance establishes a net reaction flow from ^{22}Mg to ^{24}Si . This is similar to the $2p$ capture reactions discussed in Görres et al. (1995) and Schatz et al. (1998). This type of proton capture is a weak process but goes with ρ^2 , and therefore there is a critical density above which the (α, p) reaction competes with proton captures rather than with the density independent β decay. For ^{22}Mg this happens at densities above 10^4 g cm^{-3} . As can be seen in Figure 5, the threshold for the (α, p) reaction behaves very differently in that regime because of the very different density and temperature dependence of the competing reaction. For ^{22}Mg , ^{26}Si , ^{30}S , and ^{34}Ar , the critical density is such that proton captures play an important role in determining the αp process path at these isotopes. For example, proton captures move the border for the $^{22}\text{Mg}(\alpha, p)^{25}\text{Al}$ reaction to higher temperatures, which is why the αp process needs accretion rates above $20 \dot{m}_{\text{Edd}}$ to proceed beyond ^{22}Mg . Proton captures also lead to an inversion of the thresholds for the $^{26}\text{Si}(\alpha, p)^{29}\text{P}$ and the $^{30}\text{S}(\alpha, p)^{33}\text{Cl}$ reactions for densities above 10^5 g cm^{-3} . On the other hand, in the cases of ^{14}O and ^{18}Ne the next isotone is proton unbound and the necessary densities are much higher, roughly 10^9 g cm^{-3} (Görres et al. 1995).

The solid lines in Figure 5 are the evolutionary tracks for fluid elements in the temperature-density plane at various accretion rates. The fat line segment indicates where hydrogen burning occurs (from 90% to 10% of the initial hydrogen abundance) and clearly shows that the temperature-density track for all accretion rates

crosses the threshold for the $^{15}\text{O}(\alpha,\gamma)^{19}\text{Ne}$ reaction before exhausting the hydrogen. Thus at all accretion rates, there is a breakout of the hot CNO cycle. There are uncertainties in the $^{15}\text{O}(\alpha,\gamma)^{19}\text{Ne}$ reaction rate by factors of 5–10 (Mao et al. 1995, 1996, Wiescher, Görres & Schatz 1999). However, the strong temperature dependence of the reaction rate means that changes in the reaction rate within the uncertainties have hardly any impact on the reaction flow and the breakout of the hot CNO cycle. To confirm this, we have performed a test calculation with $\dot{m}/\dot{m}_{\text{Edd}} = 0.7$ and the $^{15}\text{O}(\alpha,\gamma)^{19}\text{Ne}$ reaction rate reduced by a factor of ten. The only difference we find in this case is that the column depth of the burning zone is deeper by 8% resulting in a slightly longer CNO burning phase before the breakout. As we discuss in §5.5, this slightly increases the amount of helium that survives hydrogen burning. *Therefore we conclude that steady state hydrogen burning must always take place via the rp process.*

The time-integrated reaction flows for accretion rates of $\dot{m}/\dot{m}_{\text{Edd}} = 1, 5, 20$, and 50 are shown in Figure 6. At accretion rates below \dot{m}_{Edd} , the only important α -induced reaction (apart from the 3α process) is $^{15}\text{O}(\alpha,\gamma)^{19}\text{Ne}$, which triggers the breakout of the hot CNO cycle into the rp process starting at ^{19}Ne . The $^{14}\text{O}(\alpha,p)^{17}\text{F}$ reaction requires somewhat higher temperatures and starts to occur at $\dot{m}/\dot{m}_{\text{Edd}} \approx 1$. This reaction does not lead to a breakout of the hot CNO cycle but instead opens up another loop that proceeds via $^{17}\text{F}(p,\gamma)^{18}\text{Ne}(\beta^+)^{18}\text{F}(p,\alpha)^{15}\text{O}$. This loop just provides another path from ^{14}O to ^{15}O having the net effect of a β decay and a proton capture. The major hydrogen burning at $\dot{m} = \dot{m}_{\text{Edd}}$ still proceeds via the $^{15}\text{O}(\alpha,\gamma)^{19}\text{Ne}$ reaction and the subsequent synthesis of heavier elements via the rp process. The picture changes at higher accretion rates, however, where the $^{18}\text{Ne}(\alpha,p)^{21}\text{Na}$ reaction becomes the dominant breakout of the hot CNO cycle. The reaction flow from the CNO region towards heavier elements is then dominated by the αp process starting with the $^{14}\text{O}(\alpha,p)^{17}\text{F}$ reaction. As can be seen in Figure 5, as \dot{m} increases the ignition temperature gets higher and more (α,p) reactions become possible. This is confirmed in Figure 7, which shows the mass number of the last isotope made in the αp process $A_{\alpha p}$ as a function of \dot{m} . This mass increases with accretion rate and for $\dot{m}/\dot{m}_{\text{Edd}} = 50$ the αp process does not end until after ^{41}Sc . The rapid increase in $A_{\alpha p}$ at $\dot{m} > 15 \dot{m}_{\text{Edd}}$ reflects the small temperature differences between the thresholds for the various (α,p) reactions at $\rho > 10^5 \text{ g cm}^{-3}$ (Figure 5). The inversion of the $^{26}\text{Si}(\alpha,p)^{29}\text{P}$ and the $^{30}\text{S}(\alpha,p)^{33}\text{Cl}$ reaction thresholds is reflected in the jump in $A_{\alpha p}$ from 26 to 34 just above $20 \dot{m}_{\text{Edd}}$. As mentioned earlier, these effects are a consequence of the competition between proton captures and (α,p) reactions.

Figure 8 shows the abundances of hydrogen, helium, carbon, oxygen, nickel and the last major isotope produced in the rp process for several accretion rates as a function of time. Also shown is the abundance of one of the isotopes that dominates the composition at the end of our calculation. At $\dot{m} = \dot{m}_{\text{Edd}}$, the CNO cycle opens only at ^{15}O , which causes the slight drop in the ^{15}O abundance and the build up of ^{56}Ni after about 200 s (^{56}Ni is the first major waiting point in the rp process path). The destruction of ^{15}O is then delayed by the conversion of ^{14}O into ^{15}O via the hot CNO cycle. At higher accretion rates the opening of the CNO cycle is reflected in the rapid depletion of ^{14}O and ^{15}O with the simultaneous production of heavier nuclei like ^{56}Ni . There is a brief period of time between the breakout of the CNO cycle and the onset of the 3α reactions supplying additional CNO nuclei. This is best seen for $\dot{m} = 50 \dot{m}_{\text{Edd}}$, where the first peak in the ^{56}Ni abundance comes from processing of the initial CNO abundances, while the second peak at 20 s indicates the onset of the 3α reaction supplying more seed nuclei. The time between the breakout from the CNO cycle and helium ignition ranges from roughly 260 s at $\dot{m} = \dot{m}_{\text{Edd}}$ to 20 s at $\dot{m} = 50 \dot{m}_{\text{Edd}}$. However, the amount of hydrogen burned in this period via the rp process is only about 8–10% of the initial hydrogen abundance because of the relatively long timescales for rp processing. Therefore, helium ignition always takes place in a hydrogen-rich environment.

The build up of the last isotope in the rp process path (dot-dashed line in Figure 8) coincides with the depletion of hydrogen. The peak abundances reached for these isotopes are quite low as they are determined by the competition between production by the rp process and rapid destruction via fast β decays. Once the hydrogen is gone, the isotopes along the rp process path quickly decay into more stable isobars via a series of β decays. The resulting build up of the most abundant nuclei at the end of our calculation is shown as dotted lines in Figure 8. Some of these nuclei are still unstable and will β decay on longer timescales at greater depths.

5.2. The rp Process, Hydrogen Exhaustion and Residual Helium

The nuclei produced by helium burning are the seeds for burning the hydrogen via the rp process. As discussed above, the burning conditions are set by the point of helium ignition. For each accretion rate, the thick line segment in Figure 5 shows the region of the temperature-density plane where the hydrogen burns. The density is roughly the same for all accretion rates and increases from about 10^5 g cm^{-3} to 10^6 g cm^{-3} during the burning. On the other hand, the burning temperature depends strongly on the accretion rate and increases from $5 \times 10^8 \text{ K}$ at $\dot{m} = \dot{m}_{\text{Edd}}$ to $15\text{--}20 \times 10^8 \text{ K}$ at $\dot{m} = 50 \dot{m}_{\text{Edd}}$. The timescale for hydrogen burning is given in Table 1 and varies between 100 and 500 s.

Figure 7 shows the mass number of the rp process endpoint nucleus, A_{rp} , as a function of \dot{m} . The corresponding reaction flows for some selected cases are in Figure 6. Clearly, A_{rp} increases with \dot{m} and, for $\dot{m} > 10 \dot{m}_{\text{Edd}}$, the rp process reaches the end of our reaction network near $A = 100$. As discussed in §5.4 we expect that for accretion rates above $10 \dot{m}_{\text{Edd}}$ (but less than $50 \dot{m}_{\text{Edd}}$, see discussion below) significant amounts of nuclei heavier than $A = 100$ are produced.

The rp process reaction path in Figure 6 is characterized by a sequence of proton captures and β -decays and proceeds above ^{56}Ni along the $N = Z$ line as discussed in Schatz et al. (1998). However, we find that two-proton-capture reactions on ^{68}Se and ^{72}Kr do not play a role in steady state burning owing to the somewhat lower densities and temperatures compared to the X-ray burst peak conditions discussed in Schatz et al. (1998). Some branchings occur when proton captures are slowed down by photodisintegration or, at lower accretion rates and temperatures, because of small reaction rates. At accretion rates above $45 \dot{m}_{\text{Edd}}$ the temperatures get so high ($T_8 > 20$) that photodisintegration starts to severely hamper the rp process. At $\dot{m} = 50 \dot{m}_{\text{Edd}}$, photodisintegration of ^{84}Mo inhibits further proton captures on ^{83}Nb . As a consequence, the $^{83}\text{Nb}(p,\alpha)^{80}\text{Zr}$ reaction becomes the dominant destruction mechanism of ^{83}Nb and the rp process ends in the Zr-Nb cycle. This causes the drop in A_{rp} in Figure 7 at high \dot{m} 's. As discussed in Schatz et al. (1998) the Zr-Nb cycle occurs at high temperatures because of the very low α binding energy of ^{84}Mo . This low α binding energy is predicted by the FRDM (1992) mass model (Möller et al. 1995) used in our study. An experimental confirmation of this would be highly desirable. At accretion rates beyond $\dot{m} = 50 \dot{m}_{\text{Edd}}$, the temperatures get so high that photodisintegration drives the material into nuclear statistical equilibrium. The nuclei produced in the rp process are then quickly converted into iron peak isotopes, mostly ^{56}Ni . *It is only in this very high accretion rate regime ($\dot{m} > 50 \dot{m}_{\text{Edd}}$) that we find a pure nickel solution that will later decay to make the ashes nearly pure iron.*

What determines the endpoint of the rp process for accretion rates $\dot{m} < 50 \dot{m}_{\text{Edd}}$? The rp process ends either when all the hydrogen is consumed or when the proton capture rates become too slow because of the increasing Coulomb barrier. The effect of the Coulomb barrier can be estimated from the formula given in

Woosley and Weaver (1984)

$$Z_{\max}^{2/3} \approx \ln \left[\frac{1.5 \times 10^{11} \rho X \tau}{T_9^{2/3}} \right] \frac{T_9^{1/3}}{4.25 - 1.33 T_9^{1/3}}, \quad (14)$$

where Z_{\max} is the maximum charge number that can be synthesized in a time τ at a density ρ , a temperature T_9 (in 10^9 K) and a proton abundance X . We find that, for typical conditions during hydrogen burning and using our timescale for hydrogen burning from Table 1, the Z_{\max} is always higher than the heaviest nucleus produced in our calculations: for $\dot{m}/\dot{m}_{\text{Edd}} = 1, 5, 20, 50$ we find $Z_{\max} = 38, 45, 61$, and 92. *Therefore, the Coulomb barrier does not limit the rp process in steady state burning at high accretion rates.* This is also confirmed from the reaction flows in Figure 6. The flows are always close to the proton drip line all the way up to the heaviest nucleus synthesized, indicating that it is the β -decays and not the proton captures that set the timescale. The deviation of the rp process path from the proton drip line by 1 or 2 mass units is in most cases due to photodisintegration of the weakly-bound proton-rich nuclei.

We find that hydrogen is completely consumed by the rp process near the depth where helium ignites. No hydrogen reaches deeper regions of the atmosphere, and electron capture on hydrogen does not occur when the burning is in steady-state, as earlier speculated by Taam et al. (1996). The only exception is at very high accretion rates, typically beyond $50 \dot{m}_{\text{Edd}}$, where photodisintegration hampers efficient hydrogen burning via the rp process beyond ^{56}Ni . Indeed, Figure 6 shows that, at $\dot{m} = 50 \dot{m}_{\text{Edd}}$, there is a very weak reaction flow via hydrogen electron capture. But even at $\dot{m} = 60 \dot{m}_{\text{Edd}}$ the hydrogen mass fraction that is left after the rp process burning is 0.4%. These results contradict the speculations of Taam et al. (1996) about the possible stabilizing effects of hydrogen electron captures at large depths. A likely explanation for this is that the network of Taam et al. did not include nuclei with $A > 56$. However, from the simple arguments giving equation (13), it is clear that the rp process during steady-state burning always leads to production of nuclei beyond iron. Thus the omission of nuclei beyond $A = 56$ would result in under-consumption of hydrogen, and lead one to the incorrect conclusion that hydrogen survives the nuclear burning.

Since it is hydrogen consumption that limits the rp process, the endpoint is roughly given by equation (13). The important parameters are the endpoint of the α p process and the amount of helium burned into seed nuclei during hydrogen burning (Y_{burn}). We have shown that $A_{\alpha p}$ can in principle be obtained from Figure 5, but Y_{burn} is more difficult to estimate, since some mass fraction of helium (Y_r) survives the hydrogen burning phase (see Table 1). This helium is not available for the production of rp process seed nuclei and burns later in the pure helium burning phase discussed in §5.5.

Table 1 shows that the amount of helium surviving hydrogen burning is 23% of the initial helium abundance at $\dot{m} = \dot{m}_{\text{Edd}}$. Helium survives the hydrogen burning because the timescale to burn helium via the 3α -reaction, τ_α , is longer than the timescale for reaching the last isotope in the rp process, τ_{rp} , which is the sum of the lifetimes of all the nuclei along the calculated reaction paths. Figure 9 shows τ_α and τ_{rp} as a function of mass number for $\dot{m}/\dot{m}_{\text{Edd}} = 1$ and 20. When calculating τ_{rp} , we neglect the influence of photodisintegration and of the change in hydrogen abundance during the burning. This is a reasonable approximation since the rp process timescale is mostly set by β^+ decays. Only the proton captures at ^{52}Fe and ^{56}Ni contribute to the rp process timescale at low accretion rates. At low \dot{m} , the timescale for helium burning is indeed significantly longer than the timescale for the rp process to reach its endpoint and burn all the hydrogen. At higher accretion rates, the two timescales become comparable, and the amount of helium remaining unburned after hydrogen exhaustion is less.

5.3. The Final Abundance Distribution

The final abundance distribution of the rp process ashes from steady state burning is shown in Figure 10 for $\dot{m}/\dot{m}_{\text{Edd}} = 1, 5, 20, 50$, and 60. As discussed above, the higher the accretion rate, the heavier the nuclei produced until, at $\dot{m} = 50 \dot{m}_{\text{Edd}}$, the rp process gets stuck in the Zr-Nb cycle at $A = 80$. At this accretion rate, nuclear statistical equilibrium starts to play a role during the final burning stage, and drives some nuclei back into ^{56}Ni . These two effects lead to the “double peak” structure of the abundance pattern with maxima around $A = 56$ and $A = 80$. At $\dot{m} = 60 \dot{m}_{\text{Edd}}$, nuclear statistical equilibrium dominates and all nuclei are converted into iron peak nuclei, mainly ^{56}Ni .

The abundance distribution for $\dot{m} < 50 \dot{m}_{\text{Edd}}$ is determined by the nuclei with the slowest reaction rates in the rp process path, the so-called “waiting points” (Wallace and Woosley 1981). Some fraction of the material is locked into these waiting points until the burning is over and this leads to the production of a wide range of isotopes. The important waiting points for the conditions discussed here have been identified in Schatz et al. (1998) and are the even-even $N = Z$ nuclei ^{56}Ni , ^{64}Ge , ^{68}Se , ^{72}Kr , ^{76}Sr and ^{80}Zr . For these nuclei, proton captures are inefficient since photodisintegration or proton decay can remove a captured proton quickly and β -decay rates are relatively low. This explains the local maxima in the abundance distributions (for $\dot{m}/\dot{m}_{\text{Edd}} = 1 - 20$) at the mass numbers of these waiting point isotopes. Additional peaks occur at the nuclei that are constructed by α capture on ^{12}C as discussed in §5.5. At $\dot{m} = \dot{m}_{\text{Edd}}$, an additional peak at $A = 52$ occurs because of the relatively slow $^{52}\text{Fe}(p,\gamma)^{53}\text{Co}$ reaction rate at low temperatures (this can also be seen in Figure 9, where for low accretion rates the first major increase of the rp process timescale occurs at $A = 52$). The flat and structureless abundance distribution above $A = 72$ in the $\dot{m} = 5 \dot{m}_{\text{Edd}}$ case is caused by the fact that the rp process barely leaks beyond the major waiting points ^{68}Se and ^{72}Kr . As can be seen in Figure 6, the drastically reduced processing timescale beyond ^{72}Kr (see Schatz et al. 1998) distributes the reaction flow over a wide range of nuclei as hydrogen is rapidly depleted.

5.4. Summary of the Mixed Burning and Energy Generation

In Figure 7, we show the mass number of the last isotope reached in the α p process ($A_{\alpha p}$, open circles) and in the rp process (A_{rp} , open squares) as a function of \dot{m} . Also shown is the average mass number ($\langle A \rangle$, filled circles) and the average charge number ($\langle Z \rangle$, filled triangles) of the final composition. We now test equation (13) for accretion rates $\dot{m} < 50 \dot{m}_{\text{Edd}}$ by assuming $Y_{\text{burn}} = Y - Y_r$ and by taking Y_r from Table 1. The resulting estimated endpoints of the rp process are shown in Figure 7 as open triangles. As expected the estimated endpoint is a few mass numbers too high, since some hydrogen is burned during the beginning of the burning phase when temperatures are lower and the α p process can not yet reach its final endpoint.

Thus the estimate of equation (13) gives an upper limit to the rp process endpoint in the accretion rate regime between 15 and 45 \dot{m}_{Edd} where the reaction flow reaches the end of our network. Figure 7 shows that the heaviest nuclei that can be produced by the rp process in steady state burning are estimated to be in the $A = 150$ region. At these mass numbers the proton drip line is around $Z = 70$ and applying equation (14) we find that the Coulomb barrier should not inhibit the rp process even for these heavy nuclei. However, the endpoint of the rp process might be considerably below this upper limit because of loops in the reaction path that might occur above ^{100}Sn as the reaction path enters a region of nuclei with very low α binding energies.

To summarize, the synthesis of much heavier isotopes at higher accretion rates is not because of faster

proton capture rates, but due to enhanced (α, p) -reactions that lead to a longer αp process and therefore to heavier seed nuclei and a larger fuel to seed ratio for the rp process. The final abundance distributions as a function of mass number are shown in Figure 10 for various accretion rates. Generally, not just a single nucleus but a whole range of isotopes is produced by steady state burning. Even for our lowest accretion rate of $\dot{m} = 0.7 \dot{m}_{\text{Edd}}$ significant amounts of nuclei heavier than ^{56}Ni are synthesized.

The mixed hydrogen and helium burning is responsible for nearly all of the released nuclear energy. The energy released by the CNO cycle before helium ignition (§4) and by the helium burning after hydrogen consumption (§5.5) is negligible. Table 1 lists the energy produced by nuclear burning for different accretion rates. Hydrogen and helium are completely burned in all of our models. Because of the weak dependence of nuclear binding energy with mass number in the range of the rp process endpoints reached in this study, the released energy depends only weakly on accretion rate and burning conditions. This energy is predominantly produced by hydrogen burning. Helium burning does not contribute more than 0.6 MeV/nucleon (3α only) to 1.2 MeV/nucleon (αp process up to ^{37}K).

5.5. Helium Burning after Hydrogen Exhaustion

It was pointed out previously (in §5.2) that the relatively long timescale for helium burning allows some helium to survive the hydrogen burning phase. The mass fractions of unburned helium, Y_r , for various accretion rates are listed in Table 1. This residual helium burns later in a hydrogen-free environment via the 3α reaction and, depending on the temperature, via a series of α captures starting at ^{12}C . Figure 8 shows the build up of ^{12}C right after the hydrogen is burned, and, at accretion rates above $\dot{m} = \dot{m}_{\text{Edd}}$, the depletion of ^{12}C by the subsequent $^{12}\text{C}(\alpha, \gamma)^{16}\text{O}$ reaction. Following the $^{12}\text{C}(\alpha, \gamma)^{16}\text{O}$ reaction, a sequence of α captures occurs that can be identified in Figure 6. This α capture chain is longer for the higher temperatures at higher accretion rates, although less helium is then available (see Table 1). At $\dot{m} = 20 \dot{m}_{\text{Edd}}$, the α capture chain reaches ^{44}Ti . The nuclei produced during the pure helium burning phase can be identified in the abundance patterns shown in Figure 10 and are ^{12}C and ^{24}Mg for $\dot{m} = \dot{m}_{\text{Edd}}$, ^{12}C , ^{28}Si , and ^{32}S for $\dot{m} = 5 \dot{m}_{\text{Edd}}$ and ^{40}Ca and ^{44}Ti for $\dot{m} = 20 \dot{m}_{\text{Edd}}$.

The final mass fraction of ^{12}C for accretion rates of $\dot{m}/\dot{m}_{\text{Edd}} = 1$ and 5 is 4.1% and 0.23%, and is essentially zero for higher accretion rates. The final amount of ^{12}C is much larger at low accretion rates, because more helium is available after hydrogen exhaustion (Table 1) and at lower temperatures much less ^{12}C is destroyed by the $^{12}\text{C}(\alpha, \gamma)^{16}\text{O}$ reaction.

These conclusions depend somewhat on the rates for the CNO breakout reactions. For low accretion rates, where most ^{12}C is produced, this is the $^{15}\text{O}(\alpha, \gamma)^{19}\text{Ne}$ reaction. In principle, a lower breakout rate leads to more hydrogen burning via the hot CNO cycle, in which helium is produced (in contrast to the rp process), giving a higher final helium abundance after hydrogen burning. However, we find that a factor of ten lower $^{15}\text{O}(\alpha, \gamma)^{19}\text{Ne}$ reaction rate increases the final ^{12}C mass fraction by just 10% (a factor of ten higher rate reduces it by 25%; the uncertainty in the reaction rate is a factor of 5–10, see §5.1). We conclude that the final mass fraction of ^{12}C produced in steady state burning will never exceed 6%. It thus seems unlikely that enough ^{12}C is produced to release additional energy via explosive carbon burning deeper in the atmosphere as discussed by Brown & Bildsten (1998).

6. Conclusions

We have fully explored the complicated nucleosynthesis from thermally stable mixed hydrogen/helium burning at high accretion rates on accreting neutron stars. Our major finding is that the rp process produces a mixture of very heavy elements, the average mass of which depends on the local accretion rate.

The important reaction sequences during the mixed hydrogen and helium burning are the 3α reaction, the αp process and the rp process. For all accretion rates where the nuclear burning is in steady state, a breakout of the hot CNO cycles into the rp process takes place. It is the endpoint of the rp process that determines the energy generation and final composition of the ashes. In contradiction to Taam et al. (1996), we find that no hydrogen survives the steady state burning and consequently deep hydrogen burning by electron capture does not take place (the possibility still remains that there is substantial residual hydrogen from unstable burning in X-ray bursts). For ^{12}C the situation is similar: for accretion rates of a few times Eddington, some ^{12}C survives the burning, but never enough to trigger carbon flashes via explosive burning in deeper layers of the atmosphere.

The most important nuclear physics input parameters for our steady state burning calculations are 1) the 3α reaction rate, which triggers the burning; 2) the breakout reactions from the hot CNO cycles $^{15}\text{O}(\alpha,\gamma)^{19}\text{Ne}$ and $^{18}\text{Ne}(\alpha,p)^{21}\text{Na}$, as discussed in §5.1; 3) the (α,p) and (p,γ) - reaction rates on ^{14}O , ^{22}Mg , ^{26}Si , and ^{30}S together with the proton separation energies and the proton capture rates of ^{23}Al , ^{27}P , ^{31}Cl , and ^{35}K (these data affect the extent of helium burning and therefore the endpoint of the rp process); 4) the proton capture rates on the waiting points ^{52}Fe and ^{56}Ni ; and 5) proton capture Q-values and β -decay half lives of the even Z , $N = Z$ and the even Z , $N = Z + 1$ nuclei between ^{56}Ni and ^{100}Sn as discussed in Schatz et al. (1998). While the 3α reaction is known with sufficient accuracy, most of the other data are completely or partially based on theoretical data, for which extrapolation to the very neutron deficient nuclei in the rp process is often doubtful (see Schatz et al. 1998 for a more detailed discussion). However, while these uncertainties may affect the detailed abundance pattern for a given local accretion rate, they have no influence on our general conclusions concerning the nature of steady state burning on accreting neutron stars (see §5.1). Nevertheless, more experimental information on the nuclear data mentioned above would certainly be desirable.

Our calculations of the composition of the nuclear ashes in steady-state burning show that the ocean and crust of an accreting neutron star do not consist of pure iron, as assumed in previous work. Instead, the final composition consists of a wide range of nuclei. This is characteristic of the rp process in which some fraction of nuclei is locked at a large number of waiting points with long lifetime.

Our results will have interesting consequences for studies of the crust of accreting neutron stars. For example, our discovery of the large range of nuclei present will directly impact estimates of the thermal and electrical conductivity of the crust. To illustrate this point, we have calculated the “impurity parameter” $Q = Y_{\text{max}}^{-1} \sum_j Y_j (Z_j - Z_{\text{max}})^2$ for our models, where Y_j are the nuclear abundances and the subscript max indicates the most abundant species. We find that $Q \sim 100$ is typical of the mixture from the ashes of steady state burning. Even at very high accretion rates, ($\dot{m} \gtrsim 50 \dot{m}_{\text{Edd}}$) when nuclear statistical equilibrium favors ^{56}Ni as the sole product of nucleosynthesis, $Q \approx 1$. Brown & Bildsten (1998) showed that for $Q \geq 1$ the thermal and electrical conductivity is dominated by impurity scattering, which is strongly composition dependent. In previous work which assumed a crust of pure iron (before electron captures), impurity scattering was unimportant. Thus in accreting neutron stars, the thermal and electrical crust conductivities will be in general much lower than previously assumed, leading to a different thermal structure and faster Ohmic diffusion of magnetic fields in the crust.

We thank Ed Brown and Felix Rembges for many discussions during this work. We are especially grateful to F.-K. Thielemann and T. Rauscher for providing the reaction network solver and many of the reaction rates. This research was supported by NASA via grants NAG 5-2819 and NAGW-4517. L. B. was supported by the Hellman Family Faculty Fund Award (UCB) and the Alfred P. Sloan Foundation.

A. Radiative and Conductive Opacities

Electron scattering, free-free absorption and conduction all play a role in setting the opacity at different depths in the neutron star atmosphere. In this Appendix, we describe how we calculate each of these contributions. Prior to H/He burning, the flux in the atmosphere is carried by radiation and the opacity is set by Thomson scattering, $\kappa = \kappa_{\text{es}} = \sigma_{\text{Th}}(1 + X)/2m_p$ where X is the hydrogen mass fraction. There are corrections to κ_{es} due to degeneracy and high temperatures for which we use Paczynski's (1983) fit to the results of Buchler & Yueh (1976). This formula is valid for $\eta \equiv E_F/k_B T \lesssim 4$, where E_F is the electron Fermi energy excluding the rest mass. We find in our models that when electron scattering dominates the opacity we are safely in the $\eta \lesssim 4$ regime.

As the hydrogen and helium are burned, electrons are consumed and the average nuclear charge of the nuclei increases. This results in free-free absorption becoming much more important than electron scattering. The free-free opacity is given by

$$\kappa_{\text{ff}} = 0.753 \frac{\text{cm}^2}{\text{g}} \frac{\rho_5}{\mu_e T_8^{7/2}} \sum \frac{Z_i^2 X_i}{A_i} g_{\text{ff}}(Z_i, T, n_e), \quad (\text{A1})$$

(Clayton 1983), where the sum is over all nuclear species and $\rho_5 = \rho/10^5 \text{ g cm}^{-3}$. The dimensionless free-free Gaunt factor g_{ff} takes into account the dependence of the opacity on Coulomb wavefunction corrections, degeneracy and relativistic effects. Itoh et al. (1991) have calculated g_{ff} for pure hydrogen, helium, carbon and oxygen plasmas. So as to implement their work, we devised the fitting formula

$$g_{\text{ff}}(Z, T, n_e) = 1.16 \left[\frac{2n_Q}{n_e} \ln(1 + e^\eta) \right] \left[\frac{1 - \exp(-2\pi\gamma/\sqrt{\Pi + u})}{1 - \exp(-2\pi\gamma/\sqrt{\Pi})} \right] \left[1 + \left(\frac{T_8}{7.7} \right)^{3/2} \right], \quad (\text{A2})$$

where $\eta = E_F/k_B T$, $u = 10$,

$$\frac{2n_Q}{n_e} \equiv \frac{2(2\pi m_e k_B T)^{3/2}}{h^3 n_e} = 0.08 T_8^{3/2} \left(\frac{\mu_e}{\rho_5} \right), \quad (\text{A3})$$

$$\gamma^2 \equiv \frac{Z^2(13.6 \text{ eV})}{k_B T} = 1.58 \times 10^{-3} \frac{Z^2}{T_8}, \quad (\text{A4})$$

and

$$\Pi(\eta) \equiv [1 + \ln(1 + e^\eta)]^{2/3}. \quad (\text{A5})$$

In the regime $-2.5 < \log_{10} \gamma^2 < 2$, our fitting formula agrees with their table to better than 10% for $-6 < \eta < 5$ and 20% for $5 < \eta < 10$. In the regime $-4 < \log_{10} \gamma^2 < -2.5$ and for $-6 < \eta < 10$, the agreement is better than 20% for hydrogen and within a factor of two for oxygen. This accuracy is adequate for our application as the $\log_{10} \gamma^2 < -2.5$ regime is only relevant when the composition is mostly hydrogen, in which case electron scattering dominates. The highest Z element considered by Itoh et al. (1991) is oxygen ($Z = 8$). We assume in our work that our formula, which includes the important scalings, is applicable to

elements with greater Z . To calculate E_F , we use the analytic fitting formulae of Antia (1993) and Chabrier & Potekhin (1998, eq. [24]).

The three terms in equation (A2) are physically motivated. The first is the degeneracy correction to the electron velocity. We follow Cox & Giuli (1968, §16.2), who corrected for the electron degeneracy by integrating the free-free absorption cross-section over the Fermi-Dirac distribution. The second term is the Elwert factor (Elwert 1939); a correction to the electron wavefunction normalization due to the Coulomb potential (Pratt & Tseng 1975; Lee et al. 1976; Bethe & Salpeter 1977). The Elwert factor depends on the ratio of the Coulomb energy to the electron energy, parameterized by $\gamma^2 \equiv Z^2(13.6 \text{ eV})/k_B T$, and the energy of the photon involved in the transition. We write an average photon energy $u \equiv h\nu/k_B T$, and find that $u = 10$ gives a good fit. The parameter $\Pi(\eta)$ tracks the transition between $k_B T$ and E_F as the energy scale which sets the electron velocity. We chose the particular form of the function $\Pi(\eta)$ that gave the best fit. The third term includes the effect of relativity on the Coulomb scattering. Bethe & Salpeter (1977) show that in the extreme relativistic limit, the free-free cross section σ_{ff} is proportional to the electron energy E_e , whereas in the non-relativistic case $\sigma_{\text{ff}} \propto E_e^{-1/2}$. The Gaunt factor rises rapidly at high temperatures to allow for this different scaling, as found in the numerical calculations of Itoh and coworkers (Itoh et al. 1985, 1990, 1991; Nakagawa et al. 1987)³. We thus added a term $\propto T^{3/2}$ at high temperatures, choosing the transition temperature $T_8 = 7.7$ which gave the best fit.

The heat transport is dominated by electron conduction once the material becomes degenerate. Yakovlev & Urpin (1980, hereafter YU) wrote the conductivity as

$$K = \frac{\pi^2 k_B^2 T n_e}{3 m_* \nu_c}, \quad (\text{A6})$$

where $\nu_c = \nu_{ei} + \nu_{ee}$ is the electron collision frequency and $m_* = m_e + E_F/c^2$ (E_F is the electron Fermi energy not including the rest mass). We calculate electron-electron collisions using the fit of Potekhin et al. (1997), but these make a small contribution to the total collision frequency (typically $\lesssim 5\%$). The conductivity is mainly determined by electron-ion collisions, for which we have generalized YU's results to an ionic mixture. The scalings become evident by writing $\nu_{ei} \sim \sum_i n_i \sigma_i v_F \sim \sum_i n_i v_F Z_i^2 e^4 \Lambda_{ei} / (p_F v_F)^2$, where we sum independently over each ion and Λ_{ei} is the Coulomb logarithm. Since $v_F = p_F/m_*$ and $p_F \propto n_e^{1/3}$, we find

$$\nu_{ei} = \frac{4e^4 m_*}{3\pi \hbar^3} \frac{\sum_i Y_i Z_i^2}{Y_e} \Lambda_{ei}, \quad (\text{A7})$$

a generalized form of the familiar YU result, where $Y_i \equiv X_i/A_i$ and we have inserted the correct prefactor as found by YU. The Coulomb logarithm is

$$\Lambda_{ei} = \Lambda_{ei}^o - \frac{v_F^2}{2c^2}; \quad \Lambda_{ei}^o = \ln(r_{\text{max}}/r_{\text{min}}) \quad (\text{A8})$$

(YU), where the second term is the relativistic correction to the cross-section, and r_{max} and r_{min} are the limits of the integral over impact parameters. The lower limit is set by the electron wavelength $r_{\text{min}} = \hbar/2p_F$. YU give a good fit for the upper limit as $r_{\text{max}}^2 = r_D^2 + a^2/6$, where the Debye screening length r_D for a mixture of ions is $r_D^{-2} = 4\pi e^2 (\sum n_i Z_i^2)/k_B T$ (Shu 1991) and a is the average spacing between ions, defined

³At very high temperatures and low degeneracy, the opacity increases because of e^+e^- pair production, increasing the number density of scatterers. We never encounter this regime in our steady-state models and so do not include it here in our fitting formula.

by $4\pi a^3 \sum n_i/3 = 1$. If we also define Γ for the mixture as

$$\Gamma = \frac{e^2}{k_B T a} \frac{\sum n_i Z_i^2}{\sum n_i} = 0.49 \left(\frac{\sum_i Y_i Z_i^2}{\sum_i Y_i} \right) \frac{(\rho_7 \sum_i Y_i)^{1/3}}{T_8}, \quad (\text{A9})$$

(Hubbard & Lampe 1969), then we find

$$\Lambda_{ei}^o = \ln \left[\left(\frac{2\pi}{3} \right)^{1/3} \left(\frac{Y_e}{\sum_i Y_i} \right)^{1/3} \left(\frac{3}{\Gamma} + \frac{3}{2} \right)^{1/2} \right]. \quad (\text{A10})$$

Equation (A7), together with equations (A8), (A9) and (A10), gives a general expression for the electron-ion collision frequency for an ion mixture. For the case of a single species of ion, $\sum_i Y_i Z_i^2/Y_e = Z$ and $Y_e/\sum_i Y_i = Z$ and these equations reduce to the expressions of YU. Note that the scalings in the mixed case are *not* those obtained by substituting the mean value of Z into the expressions of YU.

In Figure 11, we show the resulting opacity for pure ^{56}Fe in the ρ - T plane. The solid lines show where the dominant opacity source changes from electron scattering to free-free absorption, and from free-free opacity to conduction, i.e. where $\kappa_{es} = \kappa_{ff}$ and $\kappa_{ff} = \kappa_{cond}$, where $\kappa_{cond} = 4acT^3/3\rho K$ is the conductive opacity. The line $\kappa_{ff} = \kappa_{cond}$ agrees well with Figure 2 of Gudmundsson, Pethick & Epstein (1983), who used the Los Alamos opacities for pure ^{56}Fe . The dotted lines show contours of total opacity κ , given by $\kappa^{-1} = \kappa_{cond}^{-1} + (\kappa_{es} + \kappa_{ff})^{-1}$. To the left of the long dashed line, significant e^+e^- pair production occurs. We do not include this in our calculations as we never encounter this regime in our steady-state models (see Figure 3), thus our opacity calculations are not valid in this region. We choose iron here as an illustrative example to compare to previous work. In practice, as we show in this paper, there is a rich mixture of elements produced by the nuclear burning.

We now compare our opacity calculations to those of previous workers. The main difference is in the treatment of free-free opacity. Taam, Woosley & Lamb (1996) in their time-dependent simulations used the KEPLER code of Weaver, Zimmerman & Woosley (1978) (see also Woosley & Weaver 1984) which calculates opacities from the analytic fits of Iben (1975). Iben (1975) provides fitting formulae to the radiative opacities of Cox & Stewart (1970a,b) and the conductive opacities of Hubbard & Lampe (1969) (for non-relativistic electrons) and Canuto (1970) (for relativistic electrons). Fujimoto and coworkers (FHM; Fujimoto et al. 1984; Hanawa & Fujimoto 1984, 1986) also used this same fit. Joss (1977), Joss & Li (1980) and Ayasli & Joss (1982) used Iben’s fit to the conductive opacity, but a fit by Stellingwerf (1975) to the radiative opacities of Cox, King & Tabor (1973). More recently, Potekhin, Chabrier & Yakovlev (1997) used the OPAL opacity library (Rogers, Swenson & Iglesias 1996) for their study of cooling neutron stars with accreted envelopes with pure H, He, C, O and Fe layers. As an example, we have compared our calculation of the total opacity κ with that obtained using the fit of Iben (1975) for the free-free contribution. We find that for pure ^{56}Fe at $\rho > 10^6 \text{ g cm}^{-3}$ and $T > 5 \times 10^8 \text{ K}$ (the ρ and T regime for which free-free opacity becomes important in our models), the total opacity we calculate is 30% to 50% larger than that using Iben’s fit.

REFERENCES

- Anders, E., & Grevesse, N. 1989, *Geochim. Cosmochim. Acta*, 53, 197
- Antia, H. M. 1993, *ApJS*, 84, 101
- Ayasli, S., & Joss, P. C. 1982, *ApJ*, 256, 637
- Bethe, H. A., & Salpeter, E. E. 1977 *Quantum Mechanics of One- and Two-Electron Atoms* (New York: Plenum)
- Bildsten, L. 1995, *ApJ*, 438, 852
- Bildsten, L., & Brown, E. F. 1997, *ApJ*, 477, 897
- Bildsten, L. 1998a, *ApJ*, 501, L89
- Bildsten, L. 1998b, in “The Many Faces of Neutron Stars”, ed. R. Buccheri, J. van Paradijs, & M. A. Alpar (Dordrecht: Kluwer), p 419
- Bildsten, L., & Cumming, A. 1998, *ApJ*, 506, 842
- Bildsten, L., & Cutler, C. 1995, *ApJ*, 449, 800
- Bildsten, L. et al. 1997, *ApJS*, 113, 367
- Bildsten, L, Salpeter, E. E., & Wasserman, I. 1992, *ApJ*, 384, 183
- Bisnovatyi-Kogan, G. S., & Chechetkin, V. M. 1979, *Sov. Phys. Usp*, 22, 89
- Blaes, O., Blandford, R., Madau, P., & Koonin, S. 1990, *ApJ*, 363, 612
- Brown, E. F., & Bildsten, L. 1998, *ApJ*, 496, 915
- Brown, E. F., Bildsten, L., & Rutledge, R. 1998, *ApJ*, 504, L95
- Buchler, J. R., & Yueh, W. R. 1976, *ApJ*, 210, 440
- Canuto, V. 1970, *ApJ*, 159, 641
- Chabrier, G., & Potekhin, A. 1998, *Phys. Rev. E*, 58, 4941
- Clayton, D. D. 1983, *Principles of Stellar Evolution and Nucleosynthesis* (Chicago: The University of Chicago Press)
- Cox, J. P., & Giuli, R. T. 1968, *Principles of Stellar Structure*, Vol. 1 (New York: Gordon & Breach)
- Cox, A. N., & Stewart, J. N., 1970a, *ApJS*, 19, 243
- Cox, A. N., & Stewart, J. N., 1970b, *ApJS*, 19, 261
- Cox, A. N., King, D. S., & Tabor, J. E. 1973, *ApJ*, 184, 201
- Elwert, G. 1939, *Ann. Phys.*, 34, 178
- Fujimoto, M. Y., Hanawa, T., & Miyaji, S. 1981, *ApJ*, 247, 267 (FHM)
- Fujimoto, M. Y., Hanawa, T., Iben I., & Richardson, M. B. 1984, *ApJ*, 278, 813
- Fuller, G. M., Fowler, W. A., & Newman, M. J. 1980 *ApJS*, 42, 447
- Fuller, G. M., Fowler, W. A., & Newman, M. J. 1982a *ApJS*, 48, 279
- Fuller, G. M., Fowler, W. A., & Newman, M. J. 1982b *ApJ*, 252, 715
- Fushiki, I., & Lamb, D. Q. 1987, *ApJ*, 323, L55
- Graboske, H. C., DeWitt, H. E., Grossman, A. S., & Cooper, M. S. 1973, *ApJ*, 181, 457

- Görres, J., Wiescher, M., & Thielemann, F.-K. 1995, *Phys. Rev. C*, 51, 392
- Gudmundsson, E. H., Pethick, C. J., & Epstein, R. I. 1983, *ApJ*, 272, 286
- Haensel, P., Kaminker, A. D., & Yakovlev, D. G. 1996, *A&A*, 314, 328
- Haensel, P., & Zdunik, J. L. 1990a, *A&A*, 227, 431
- Haensel, P., & Zdunik, J. L. 1990b, *A&A*, 229, 117
- Hanawa, T., & Fujimoto, M. Y. 1984, *PASJ*, 36, 199
- Hanawa, T., & Fujimoto, M. Y. 1986, *PASJ*, 38, 13
- Hanawa, T., Sugimoto, D., & Hashimoto, M. 1983, *PASJ*, 35, 491
- Hasinger, G., & van der Klis, M. 1989, *A&A*, 225, 79
- Herndl, H., Görres, J., Wiescher, M., Brown, B. A., & Van Wormer, L. 1995, *Phys. Rev. C* 52, 1078
- Hoyle, R. & Fowler, W. A. 1965, in “Quasi-Stellar Sources and Gravitational Collapse”, ed. Robinson, I., Schild, A., & Schucking, E. L. (Chicago: University of Chicago Press), p. 17
- Hubbard, W. B., & Lampe, M. 1969, *ApJS*, 18, 297
- Iben, I., Jr. 1975, *ApJ*, 196, 525
- Itoh, N., Totsuji, H., Ichimaru, S., & DeWitt, H. E. 1979, *ApJ*, 234, 1079
- Itoh, N., Kohyama, Y., & Nozawa, S. 1985, *ApJ*, 294, 17
- Itoh, N., Kojo, K., & Nakagawa, M. 1990, *ApJS*, 74, 291
- Itoh, N., Kuwashima, F., Ichihashi, K., & Mutoh, H. 1991, *ApJ*, 382, 636
- Joss, P. C. 1977, *Nature*, 270, 310
- Joss, P. C., & Li, F. K. 1980, *ApJ*, 238, 287
- Koike, O., Hashimoto, M., Arai, K., & Wanajo, S. 1999, *A&A*, 342, 464
- Lamb, D. Q., & Lamb, F. K. 1978, *ApJ*, 220, 291
- Lee, C. M., Kissel, L., Pratt, R. H., & Tseng, H. K. 1976, *Phys. Rev. A*, 13, 1714
- Lewin, W. H. G., van Paradijs, J., & Taam, R. E. 1995, in “X-Ray Binaries”, ed. W. H. G. Lewin, J. van Paradijs, J., & E. van den Heuvel (London: Cambridge) p. 175
- Mao, Z. Q., Fortune, H. T., & Lacaze, A. G. 1995, *Phys. Rev. Lett.*, 74, 3760
- Mao, Z. Q., Fortune, H. T., & Lacaze, A. G. 1996, *Phys. Rev. C*, 53, 1197
- Miralda-Escude, J., Paczynski, B., & Haensel, P. 1990, *ApJ*, 362, 572
- Möller, P., Nix, J. R., Myers, W. D., & Swiatecki, W. J. 1995, *At. Data Nucl. Data Tab.*, 59, 185
- Nakagawa, M., Kohyama, Y., & Itoh, N. 1987, *ApJS*, 63, 661
- Paczynski, B. 1983, *ApJ*, 267, 315
- Pethick, C. J., & Ravenhall, D. G. 1995, *Ann. Rev. Nucl. Part. Sci.*, 45, 429
- Potekhin, A. Y., Chabrier, G., & Yakovlev, D. G. 1997, *A&A*, 323, 415
- Pratt, R. H., & Tseng, H. K. 1975, *Phys. Rev. A*, 11, 1797
- Ravenhall, D. G., & Pethick, C. J. 1994, *ApJ*, 424, 846
- Rogers F. J., Swenson, F. J., & Iglesias, C. A. 1996, *ApJ*, 456, 902

- Sato, K. 1979, *Prog. of Theor. Physics*, 62, 957
- Schatz, H. et al. 1998, *Phys. Rep.*, 294, 167
- Schatz, H., Bildsten, L., Gorres, J., Wiescher, M., & Thielemann, F.-K. 1997, in “Intersections Between Particle and Nuclear Physics”, ed. T. W. Donnelly (New York: AIP), p. 987
- Shu, F. H. 1991, *The Physics of Astrophysics Vol.1 : Radiation* (CA: University Science Books)
- Stellingwerf, R. F. 1975, *ApJ*, 195, 441
- Taam, R. E. 1981, *Ap&SS*, 77, 257
- Taam, R. E. 1982, *ApJ*, 258, 761
- Taam, R. E., & Picklum, R. E. 1978, *ApJ*, 224, 210
- Taam, R. E., & Picklum, R. E. 1979, *ApJ*, 233, 327
- Taam, R. E., Woosley, S. E., & Lamb, D. Q. 1996, *ApJ*, 459, 271
- Van Wormer, L., Görres, J., Iliadis, C., Wiescher, M., & Thielemann, F.-K. 1994, *ApJ*, 432, 326
- Wallace, R. K., & Woosley, S. E. 1981, *ApJS*, 45, 389
- Wallace, R. K., Woosley, S. E., & Weaver, T. A. 1982, *ApJ*, 258, 696
- Wallace, R. K., & Woosley, S. E. 1984, in “High Energy Transients in Astrophysics”, ed. S. E. Woosley (New York: AIP), p. 319
- Weaver, T. A., Zimmerman, G. B., & Woosley, S. E. 1978, *ApJ*, 225, 1021
- Wiescher, M., Görres, J., & Schatz, H. 1999, *Journal of Phys. G*, Topical Review, submitted
- Wiescher, M., Görres, J., Thielemann, F.-K., & Ritter, H. 1986, *A&A*, 160, 56
- Woosley, S. E., & Weaver, T. A. 1984, in “High Energy Transients in Astrophysics”, ed. S. E. Woosley (New York: AIP), p. 273
- Yakovlev, D. G., & Urpin, V. A. 1980, *Soviet Astron.*, 24, 303

Table 1. H-burning Duration, Energy Generation, and Amount of Helium Surviving H-burning

$\dot{m}/\dot{m}_{\text{Edd}}$	t_{H} (s) ^a	E (MeV/nucleon) ^b	Y_r (%) ^c
1	486	5.34	6.7
5	185	5.61	4.5
20	109	5.65	2.9
50	349	5.98	1.4

^aThe time for the hydrogen abundance to decrease from 90% to 10% of its initial value.

^bThe total energy release from the nuclear burning.

^cThe mass fraction of helium that remains when 99% of the hydrogen has been burned.

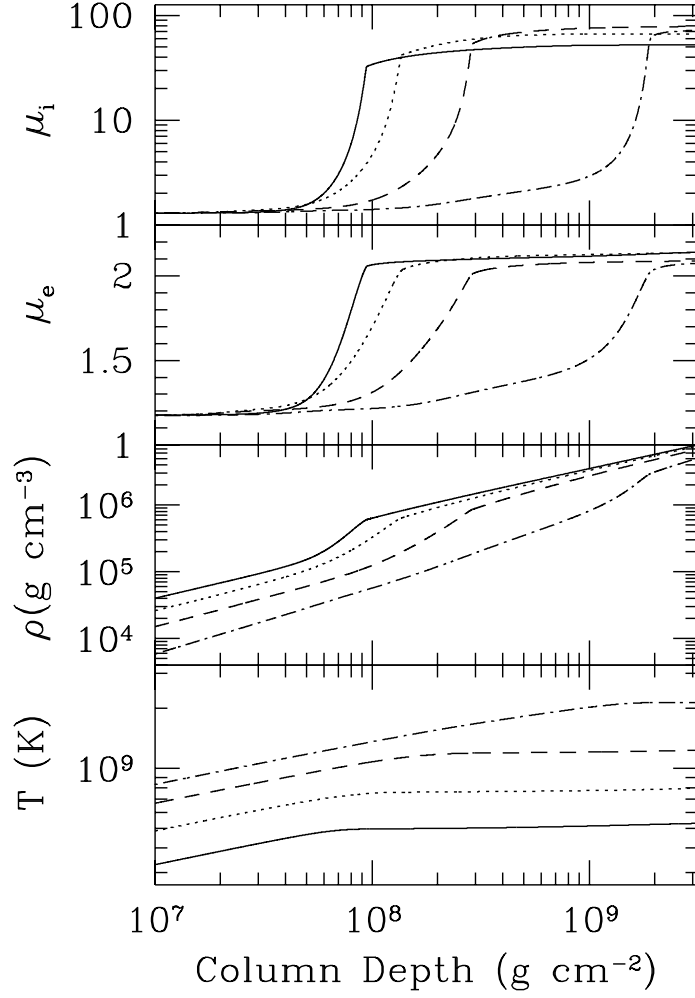


Fig. 1.— The structure of a rapidly accreting $M = 1.4M_{\odot}$, $R = 10$ km neutron star atmosphere which is burning its fuel in steady-state. The plots show the ion mean molecular weight (μ_i), electron mean molecular weight (μ_e), density and temperature as a function of the column depth into the star. The solid, dotted, dashed and dot-dashed lines are for $\dot{m}/\dot{m}_{\text{Edd}} = 1, 5, 20$ and 50 , respectively.

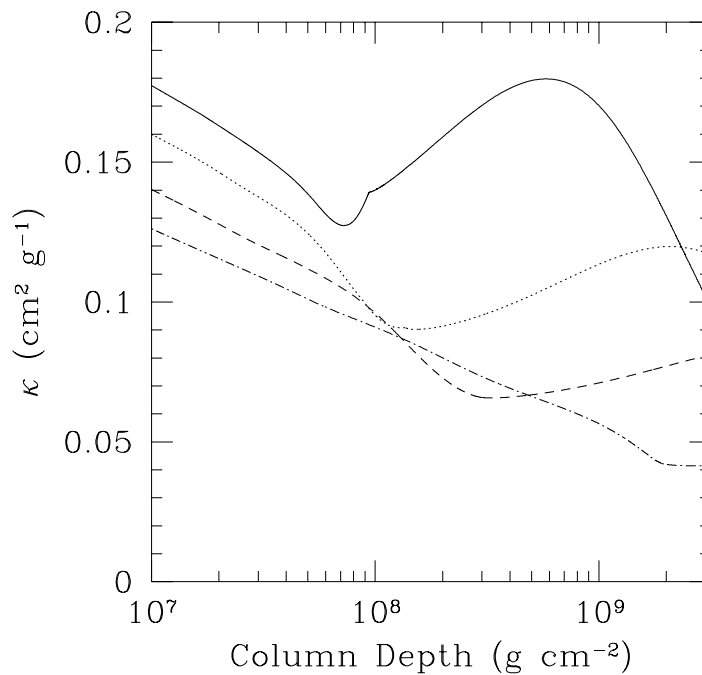


Fig. 2.— The total opacity κ as a function of column depth for the models shown in Figure 1 and described in § 4. The solid, dotted, dashed and dot-dashed lines are for $\dot{m}/\dot{m}_{Edd} = 1, 5, 20$ and 50 respectively. Above the burning layer, the opacity is mainly electron scattering. After the main hydrogen burning occurs, free-free absorption dominates the opacity until conduction by the degenerate electrons becomes the main heat transport mechanism. This gives a “bump” in the opacity, particularly prominent at low accretion rates.

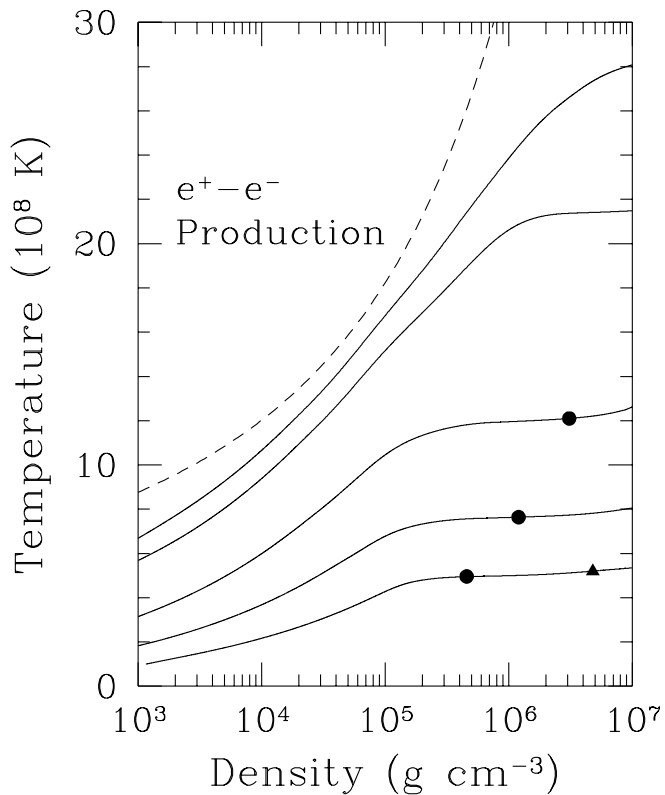


Fig. 3.— The temperature-density profiles of a rapidly accreting $M = 1.4M_{\odot}$, $R = 10$ km neutron star atmosphere which is burning in steady-state. From bottom to top, the curves are for $\dot{m}/\dot{m}_{\text{Edd}} = 1, 5, 20, 50$ and 60, respectively. The number density of positrons exceeds 10% of the neutralizing electron density to the left of the dashed line. For this reason, we do not go above $\dot{m}/\dot{m}_{\text{Edd}} = 60$. To the left of the filled circle, the opacity is set by electron scattering ($\kappa_{es} > \kappa_{ff}$); to the right of this point, free-free opacity is more important ($\kappa_{ff} > \kappa_{es}$). Conduction eventually takes over from radiation as the heat transport mechanism. For the $\dot{m} = \dot{m}_{\text{Edd}}$ model, we mark with a triangle where $\kappa_{\text{cond}} = \kappa_{ff}$ (for the other models, conduction takes over at $\rho > 10^7$ g cm $^{-3}$).

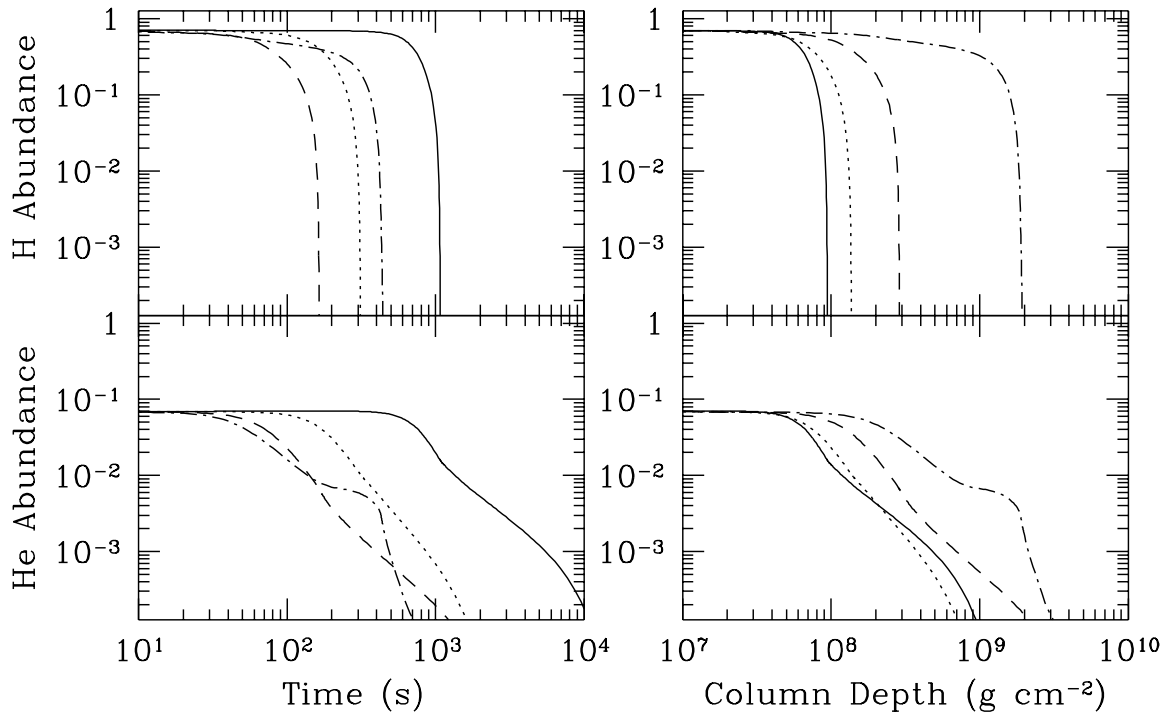


Fig. 4.— Hydrogen and helium abundances as a function of time (left panel) and column depth (right panel) for accretion rates $\dot{m}/\dot{m}_{\text{Edd}} = 1$ (solid line), 5 (dotted line), 20 (dashed line), and 50 (dot-dashed line).

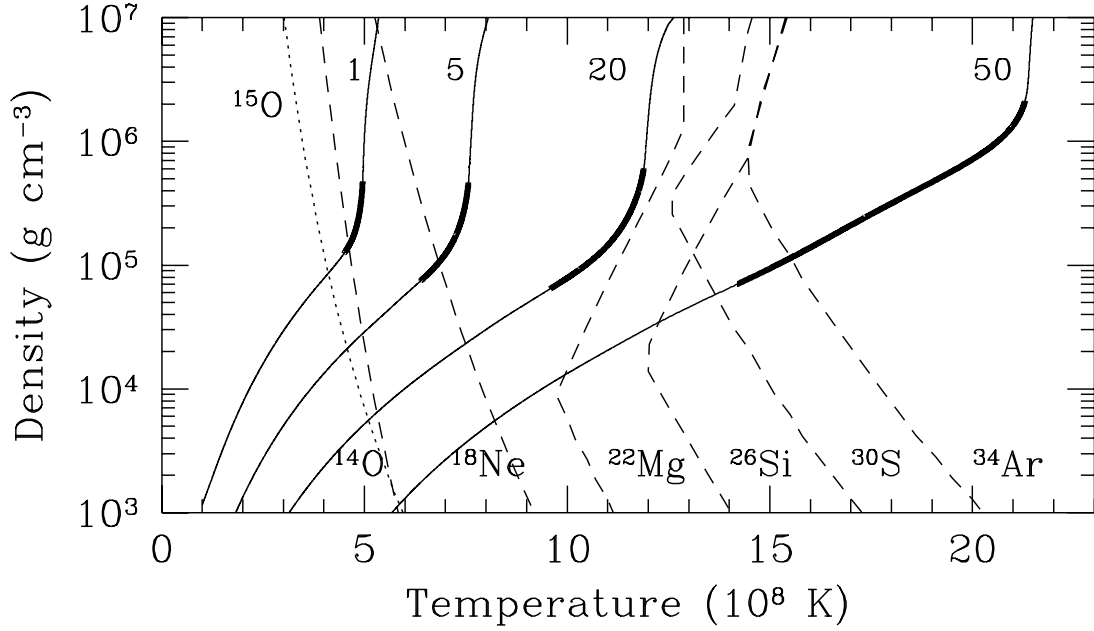


Fig. 5.— The tracks of a fluid element in the T - ρ plane for various accretion rates. The accretion rate is indicated by the number near the end of the track in units of \dot{m}_{Edd} . The thick line segment shows where hydrogen burns from 90% down to 10% of its initial abundance. The dotted line marked “ ^{15}O ” shows the conditions where the $^{15}\text{O}(\alpha, \gamma)^{19}\text{Ne}$ rate equals the ^{15}O β^+ decay rate. The dashed lines show where the (α, p) reaction rates on ^{14}O , ^{18}Ne , ^{22}Mg , ^{26}Si , ^{30}S and ^{34}Ar equal the other destruction mechanisms (β^+ decays and proton captures) on these isotopes. In the temperature and density region to the right of these dashed (or dotted) lines, the (α, p) (or (α, γ)) reactions dominate the destruction reactions of the respective isotopes.

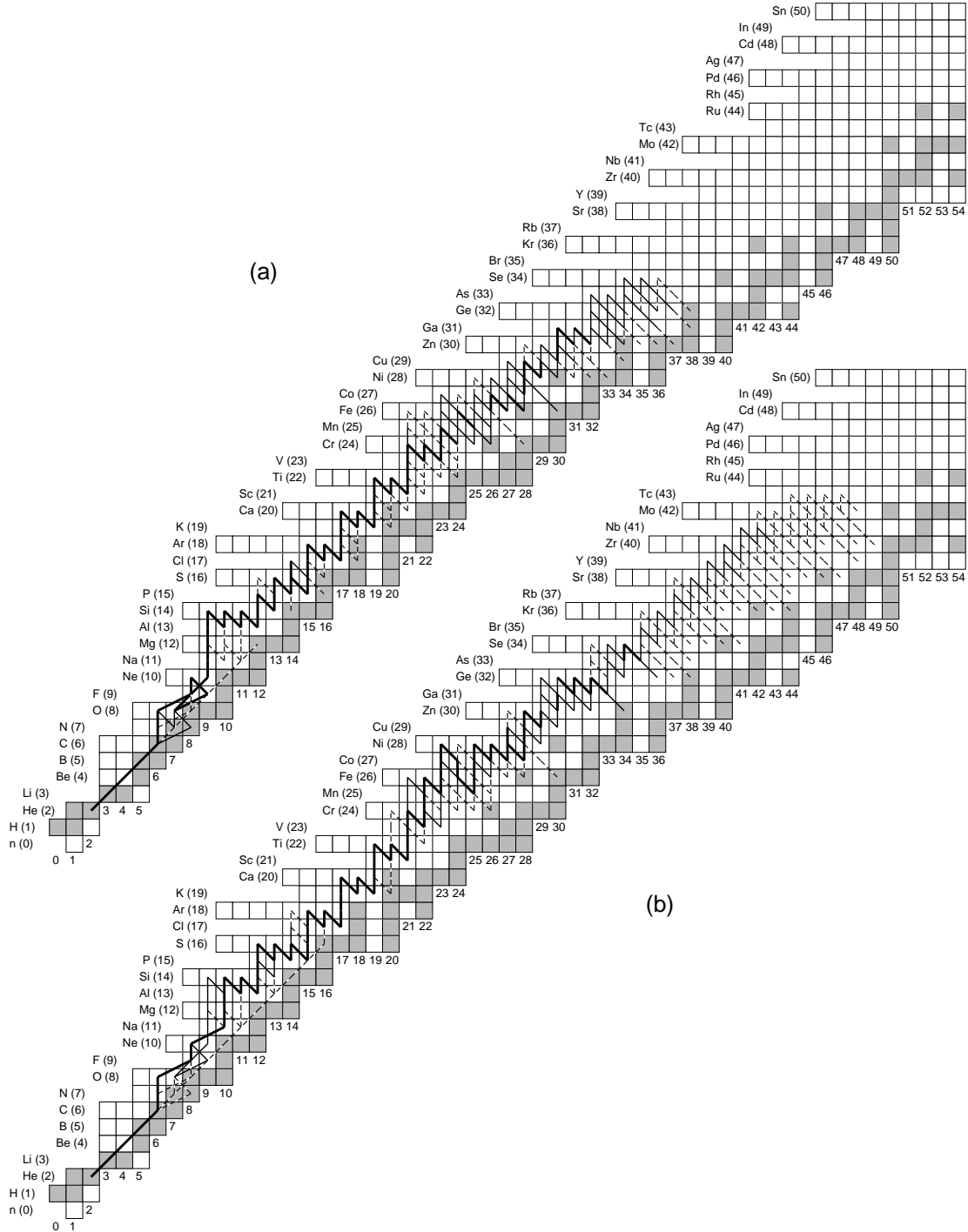


Fig. 6.— The time-integrated reaction flow for accretion rates of (a) $1 \dot{m}_{\text{Edd}}$, (b) $5 \dot{m}_{\text{Edd}}$, (c) $20 \dot{m}_{\text{Edd}}$ and (d) $50 \dot{m}_{\text{Edd}}$. The thickness of each line indicates the strength of the reaction flow relative to the 3α -reaction: more than 50% flow (thick solid line), 10%–50% flow (thin solid line), and 1%–10% flow (dashed line). The 3α reaction is a useful normalization reaction since essentially all the reaction flow passes through that reaction for all accretion rates. Each square stands for a proton stable nucleus, filled squares are stable nuclei and “P” indicates a p-nucleus. Nuclei on the neutron rich side of stability have been omitted.

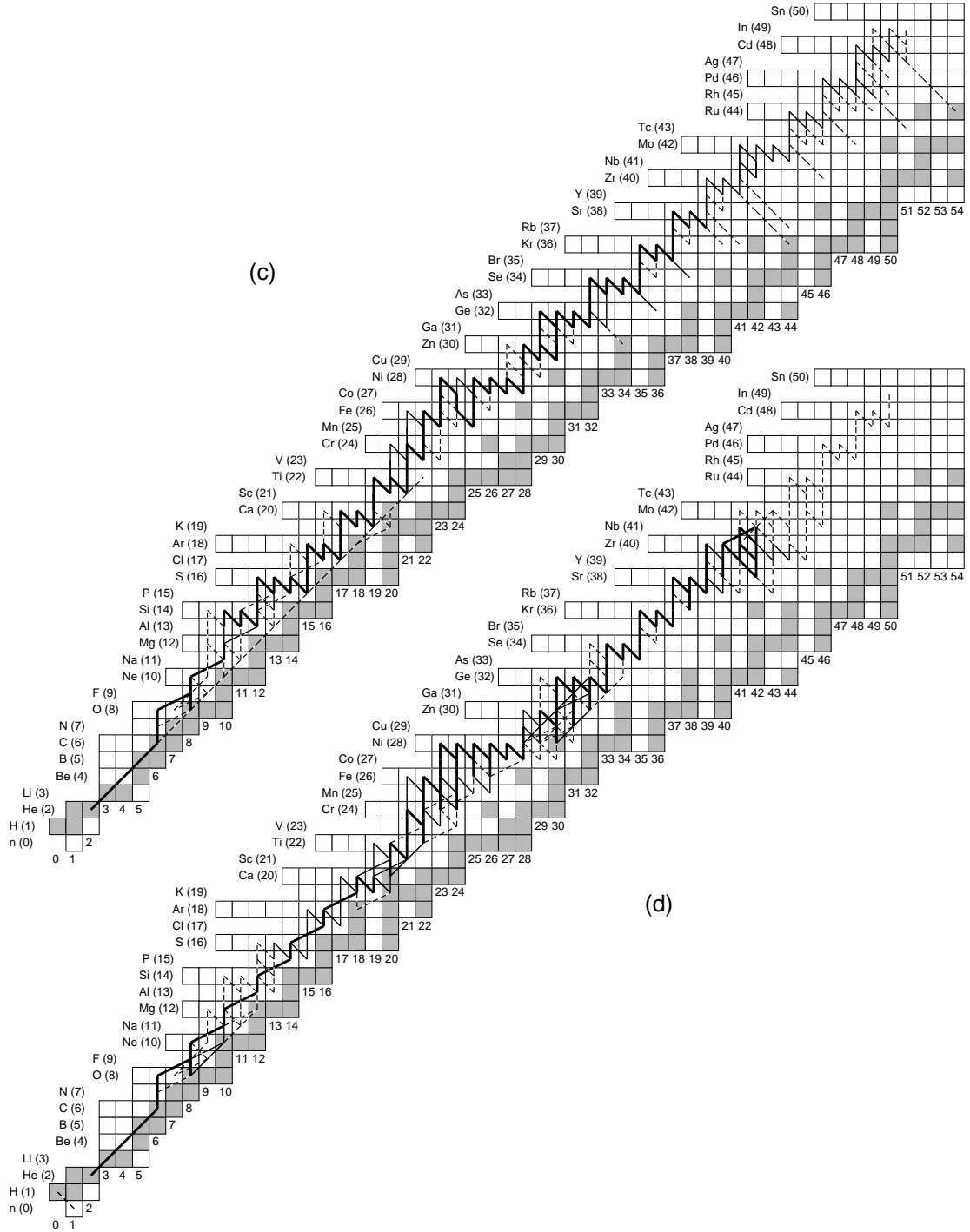


Fig. 6.— Continued.

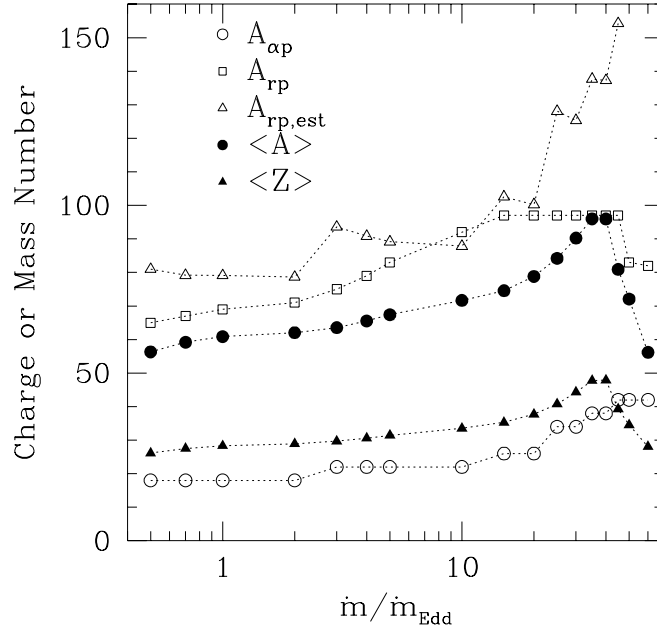


Fig. 7.— The mass number of the last isotope produced in the αp process ($A_{\alpha p}$, open circles) and in the rp process (A_{rp} , open squares) as a function of the local accretion rate $\dot{m}/\dot{m}_{\text{Edd}}$. The last isotope produced is defined as the isotope where the time integrated reaction flow of the respective process drops below 10% of its maximum. The open triangles show $A_{rp,est}$, the estimate of A_{rp} from $A_{\alpha p}$ using equation (13). We also show the average mass number ($\langle A \rangle$, filled circles) and the average charge number ($\langle Z \rangle$, filled triangles) of the final composition (excluding nuclei with $A \leq 12$). We connect the data points with straight lines to guide the eye.

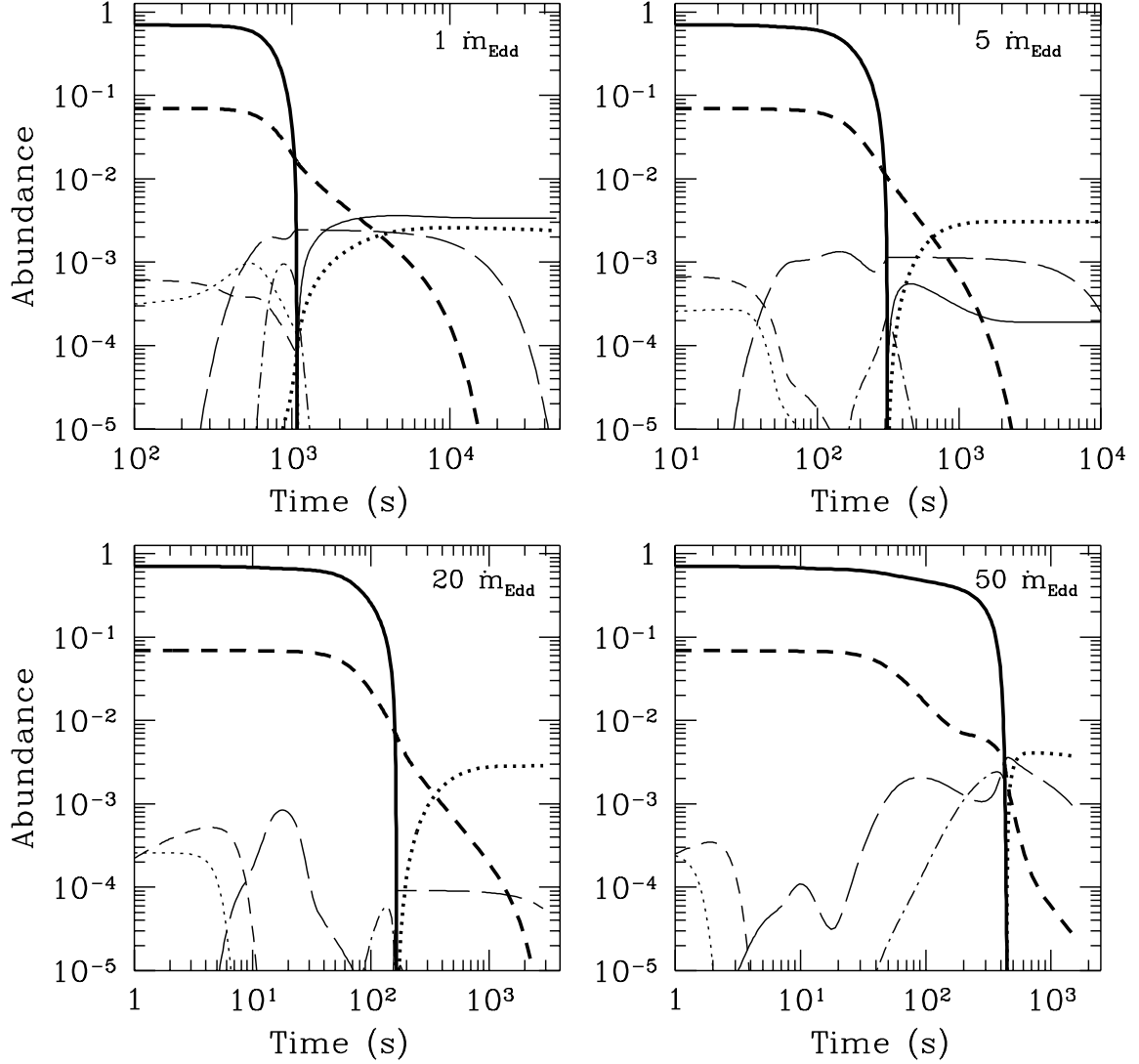


Fig. 8.— The abundances of various isotopes as a function of time for accretion rates $\dot{m}/\dot{m}_{\text{Edd}}=1, 5, 20$, and 50. In each figure, we show abundances of ^1H (bold solid line), ^4He (bold dashed line), ^{12}C (solid line), ^{14}O (dotted line), ^{15}O (short dashed line) and ^{56}Ni (long dashed line). The dot-dashed line shows the last isotope produced by the rp process in each case. This is ^{67}As , ^{80}Y , ^{96}Cd and ^{80}Zr for $\dot{m}/\dot{m}_{\text{Edd}}=1, 5, 20$, and 50 respectively. The thick dotted line shows an abundant element in each case at the end of our calculations. This is ^{67}Ga , ^{64}Zn , ^{68}Ge and ^{80}Sr for $\dot{m}/\dot{m}_{\text{Edd}}=1, 5, 20$, and 50 respectively.

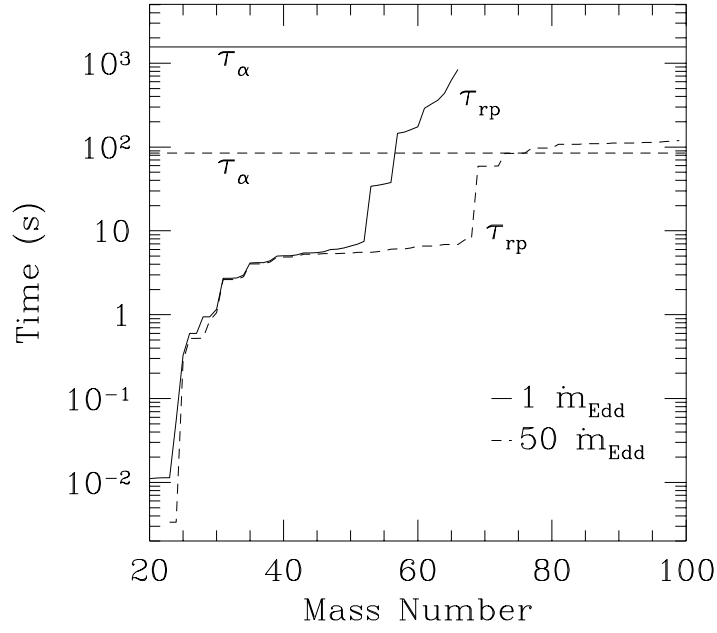


Fig. 9.— The time it takes the rp process to reach a given mass number τ_{rp} compared to the timescale for helium burning via the 3α -reaction τ_α . We show results for two different accretion rates: $\dot{m} = \dot{m}_{\text{Edd}}$ (solid lines) and $\dot{m} = 50\dot{m}_{\text{Edd}}$ (dashed lines). For $\dot{m} = \dot{m}_{\text{Edd}}$, $\tau_{\text{rp}} \ll \tau_\alpha$, whereas for $\dot{m} = 50 \dot{m}_{\text{Edd}}$ the timescales become comparable for $A \gtrsim 70$. This explains why the amount of helium remaining when hydrogen is exhausted (Y_r) is less for higher accretion rates (Table 1).

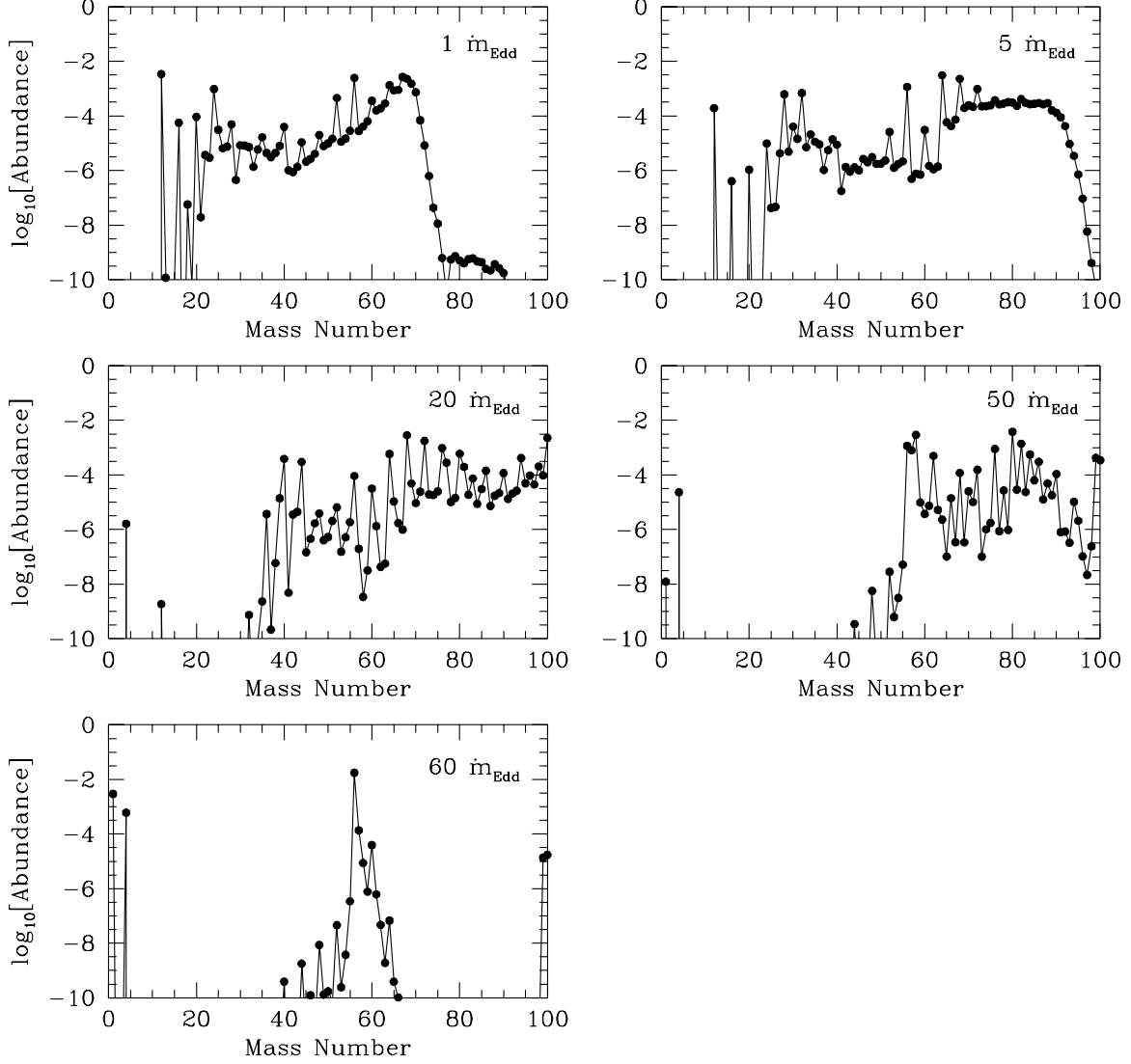


Fig. 10.— The distribution of the final abundances for accretion rates of $\dot{m}/\dot{m}_{\text{Edd}}=1, 5, 20, 50$ and 60 . The final isotopic abundances have been summed for each mass number A and the resulting abundances are shown as functions of A .

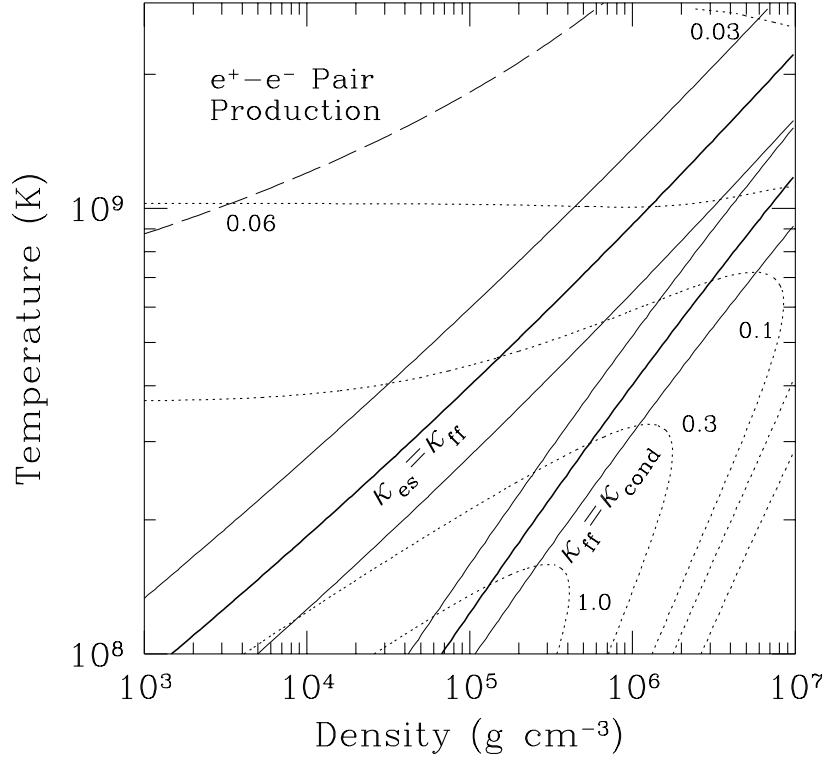


Fig. 11.— Contours of opacity for pure ⁵⁶Fe in the ρ - T plane (dotted lines). Each contour is labelled with the value of opacity κ . The heavy solid lines show where the contributions due to conduction (κ_{cond}) or electron scattering (κ_{es}) are equal to the free-free opacity κ_{ff} . The light solid lines show where the ratios κ_{ff}/κ_{es} or $\kappa_{ff}/\kappa_{cond}$ are equal to 0.25 or 4. The number density of positrons exceeds 10% of the neutralizing electron density to the left of the dashed line: our opacity calculations are not valid in this region (we do not encounter this regime in our models).